

NASA Contractor Report 191474

11N-15
169408
P.97

Moment Method Analysis of Linearly Tapered Slot Antennas

Adnan Köksal

*North Carolina State University
Raleigh, North Carolina*

Grant NAG1-943
June 1993

(NASA-CR-191474) MOMENT METHOD
ANALYSIS OF LINEARLY TAPERED SLOT
ANTENNAS Final Report, 15 Jan. 1989
- 30 Sep. 1991 (North Carolina
State Univ.) 97 p

N93-27261

Unclas

G3/15 0169408



National Aeronautics and
Space Administration

Langley Research Center
Hampton, Virginia 23681-0001

**Moment Method Analysis of
Linearly Tapered Slot Antennas**

by

Adnan Köksal

**Low Loss Components for Switched Beam Radiometers
Final Report**

NASA Grant No: NAG-1-943

Covering the period

Jan. 15, 1989 to Sept. 30, 1991

Co-Principal Investigators: Robert J. Trew
J. Frank Kauffman

**Department of Electrical and Computer Engineering
North Carolina State University**

Raleigh, NC

Abstract

A Method of Moments (MoM) model for the analysis of the Linearly Tapered Slot Antenna (LTSA) is developed and implemented. The model employs an unequal size rectangular sectioning for conducting parts of the antenna. Piecewise sinusoidal basis functions are used for the expansion of conductor current. The effect of the dielectric is incorporated in the model by using equivalent volume polarization current density and solving the equivalent problem in free-space. The feed section of the antenna including the microstripline is handled rigorously in the MoM model by including slotline short-circuit and microstripline currents among the unknowns. Comparison with measurements is made to demonstrate the validity of the model for both the air case and the dielectric case. Validity of the model is also verified by extending the model to handle the analysis of the skew-plate antenna, and comparing the results to those of a skew-segmentation modeling results of the same structure and to available data in the literature. Variation of the radiation pattern for the air LTSA with length, height and taper angle is investigated and the results are tabulated. Numerical results for the effect of the dielectric thickness and permittivity are presented.

Table of Contents

List of Tables	v
List of Figures	vi
1 INTRODUCTION	1
1.1 Problem Statement and Objectives	1
1.2 Significance	3
1.3 Background	4
1.4 Overview of Report	8
2 FORMULATION OF THE METHOD	10
2.1 Introduction	10
2.2 Derivation of the Integral Equations	12
2.3 Solution of the Integral Equations by the Method of Moments	17
3 IMPLEMENTATION OF THE METHOD FOR LINEARLY TA- PERED SLOT ANTENNA	21
3.1 Introduction	21

3.2	Conductor Modeling	22
3.3	Conductor Basis and Test Functions	24
3.4	Dielectric Modeling	28
3.5	Dielectric Basis and Test Functions	29
3.6	Source Modeling	31
3.7	Evaluation of the Matrix Equation	34
3.8	Solution of the Matrix Equation	38
4	RESULTS AND DISCUSSION	42
4.1	Introduction	42
4.2	Verification of Computed Results	45
4.3	Computed Results for Air Tapered Slot Antennas	58
4.4	Computed Results for Dielectric Tapered Slot Antennas	65
5	COMPUTER CODE AND PERFORMANCE	70
5.1	Code	70
5.2	CPU Time and Memory Requirements	70
6	CONCLUSIONS AND SUGGESTIONS FOR FUTURE WORK	76
	REFERENCES	81
A		86
A.1	Introduction	87
A.2	Preparation of ltsa	87

A.3 Running ltsa and pattern programs	87
A.4 Input File Organization and Variables	88
A.5 Listing of Programs	93

List of Tables

4.1 Results for the air LTSA study	60
--	----

List of Figures

1.1	LTSA Geometry	2
1.2	Skew-Plate antenna	7
2.1	Scattering Problem Geometry	10
2.2	Equivalent Problem	14
3.1	LTSA Geometry	21
3.2	Unequal Size Rectangular Sectioning	23
3.3	Piecewise Sinusoidal Conductor Currents a) Segment geometry b) Dis- tribution in Current Direction c) Distribution in Perpendicular Direction	25
3.4	Parallel Monopoles	27
3.5	Perpendicular Monopoles	28
3.6	Dielectric Segmentation	29
3.7	Possible Source Configurations of the LTSA a) Receiving mode with a detector diode b) LTSA with a microstripline to slotline transition . .	32
3.8	Geometry of conductor and dielectric currents	36
4.1	E-Plane of the LTSA	43

4.2	H-Plane of the LTSA	43
4.3	Antenna configurations a) LTSA positioning, b) Standard gain antenna positioning.	46
4.4	Comparison of E-Plane radiation patterns for skew-plate and unequal-size rectangular modeling ($L = 1.0\lambda_0$, $H = 0.5\lambda_0$, $W_f = 0.004\lambda_0$, $\alpha = 5$ degrees).	47
4.5	Comparison of H-Plane radiation patterns for skew-plate and unequal-size rectangular modeling ($L = 1.0\lambda_0$, $H = 0.5\lambda_0$, $W_f = 0.004\lambda_0$, $\alpha = 5$ degrees).	47
4.6	E-Plane radiation pattern for a skew-plate antenna with two different segmentation ($L = 5.2\lambda_0$, $H = 0.9\lambda_0$, $W_f = 0.06\lambda_0$, $\alpha = 7$ degrees). . .	48
4.7	H-Plane radiation pattern for a skew-plate antenna with two different segmentation ($L = 5.2\lambda_0$, $H = 0.9\lambda_0$, $W_f = 0.06\lambda_0$, $\alpha = 7$ degrees). . .	49
4.8	Magnitude of antenna current along $z = 0.75\lambda_0$. — : J_z , - - - : J_x . . .	50
4.9	Phase of antenna current along $z = 0.75\lambda_0$. — : J_z , - - - : J_x	51
4.10	Magnitude of antenna current along $x = 2.53\lambda_0$. — : J_z , - - - : J_x . . .	51
4.11	Phase of antenna current along $x = 2.53\lambda_0$. — : J_z , - - - : J_x	52
4.12	Feed design of the test antenna	53
4.13	Measured and computed co-polar radiation patterns for LTSA in air ($L = 5.5\lambda_0$, $L_i = 0.5\lambda_0$, $H = 1.5\lambda_0$, $W_f = 0.02\lambda_0$, $\alpha = 7$ degrees). . . .	54

4.14 Measured and computed co-polar and cross polar D-Plane radiation pattern for LTSA in air ($L = 5.5\lambda_0$, $L_i = 0.5\lambda_0$, $H = 1.5\lambda_0$, $W_f = 0.02\lambda_0$, $\alpha = 7$ degrees).	55
4.15 Measured and computed co-polar E and H-Plane radiation patterns for a dielectric LTSA ($\epsilon_r = 2.33$, $d = 0.02362\lambda_0$, $L = 5.5\lambda_0$, $L_i = 0.5\lambda_0$, $H = 1.5\lambda_0$, $W_f = 0.02\lambda_0$, $\alpha = 7$ degrees).	57
4.16 Measured and computed co-polar and cross-polar D-Plane radiation patterns for a dielectric LTSA ($\epsilon_r = 2.33$, $d = 0.02362\lambda_0$, $L = 5.5\lambda_0$, $L_i = 0.5\lambda_0$, $H = 1.5\lambda_0$, $W_f = 0.02\lambda_0$, $\alpha = 7$ degrees).	57
4.17 Variation of E and H -Plane patterns of LTSA's with H .	61
4.18 Variation of D -Plane pattern of LTSA's with H .	61
4.19 Variation of E and H -Plane patterns of LTSA's with α .	62
4.20 Variation of D -Plane pattern of LTSA's with α .	63
4.21 Variation of E and H -Plane patterns of LTSA's with L .	64
4.22 Variation of D -Plane pattern of LTSA's with L .	65
4.23 Variation of the E-Plane pattern for LTSA's with ϵ_r . A: $\epsilon_r = 2.33$, B: $\epsilon_r = 4.0$, C: $\epsilon_r = 5.0$ ($L = 2.0\lambda_0$, $H = 0.4\lambda_0$, $W_f = 0.01\lambda_0$, $d = 0.03\lambda_0$, $\alpha = 5$ degrees).	66
4.24 Variation of the H-Plane pattern for LTSA's with ϵ_r . A: $\epsilon_r = 2.33$, B: $\epsilon_r = 4.0$, C: $\epsilon_r = 5.0$ ($L = 2.0\lambda_0$, $H = 0.4\lambda_0$, $W_f = 0.01\lambda_0$, $d = 0.03\lambda_0$, $\alpha = 5$ degrees).	67

4.25	Variation of the E-Plane pattern for LTSA's with dielectric thickness, <i>d</i> . A: $d = 0.02\lambda_0$, B: $d = 0.06\lambda_0$, C: $d = 0.1\lambda_0$ ($\epsilon_r = 2.33$, $L = 2.0\lambda_0$, $H = 0.4\lambda_0$, $W_f = 0.01\lambda_0$, $\alpha = 5$ degrees).	67
4.26	Variation of the H-Plane pattern for LTSA's with dielectric thickness, <i>d</i> . A: $d = 0.02\lambda_0$, B: $d = 0.06\lambda_0$, C: $d = 0.1\lambda_0$ ($\epsilon_r = 2.33$, $L = 2.0\lambda_0$, $H = 0.4\lambda_0$, $W_f = 0.01\lambda_0$, $\alpha = 5$ degrees).	68
4.27	Variation of the E-Plane pattern for LTSA's with dielectric thickness, <i>d</i> , high ϵ_r case. A: $d = 0.02\lambda_0$, B: $d = 0.04\lambda_0$ ($\epsilon_r = 9.8$, $L = 1.05\lambda_0$, $H = 0.38\lambda_0$, $W_f = 0.004\lambda_0$, $\alpha = 5.7$ degrees).	69
4.28	Variation of the H-Plane pattern for LTSA's with dielectric thickness, <i>d</i> , high ϵ_r case. A: $d = 0.02\lambda_0$, B: $d = 0.04\lambda_0$ ($\epsilon_r = 9.8$, $L = 1.05\lambda_0$, $H = 0.38\lambda_0$, $W_f = 0.004\lambda_0$, $\alpha = 5.7$ degrees).	69
5.1	Block Diagram of the Code	71
5.2	Matrix fill-time and solve time on Alliant FX-40 for air LTSA's . . .	73
5.3	Total CPU time comparison for air LTSA's	74
5.4	CPU time on CRAY Y-MP for dielectric LTSA's	74

CHAPTER 1

INTRODUCTION

1.1 Problem Statement and Objectives

The main objective of this work is to develop a Moment Method Model for the radiation pattern characterization of single Linearly Tapered Slot Antennas (LTSA) in air or on a dielectric substrate. The geometry of the LTSA is shown in Figure 1.1.

This characterization consists of:

- Finding the radiated far-fields of the antenna,
- Determining the *E*-Plane and *H*-Plane beamwidths and sidelobe levels,
- Determining the *D*-Plane beamwidth and cross polarization levels,

as antenna parameters length (L), height (H), taper angle (α), substrate thickness (d) and the relative substrate permittivity (ϵ_r) vary. The ranges of these parameters are:

$$0.25\lambda_0 \leq L \leq 5\lambda_0$$

$$0.25\lambda_0 \leq H \leq 3\lambda_0$$

$$2.5 \text{ deg} \leq \alpha \leq 9 \text{ deg}$$

$$0.01\lambda_0 \leq d \leq 0.1\lambda_0$$

$$1 \leq \epsilon_r \leq 10.5$$

where λ_0 is the free-space wavelength at the operating frequency.

The reason for these choices of parameter ranges will be explained in later sections.

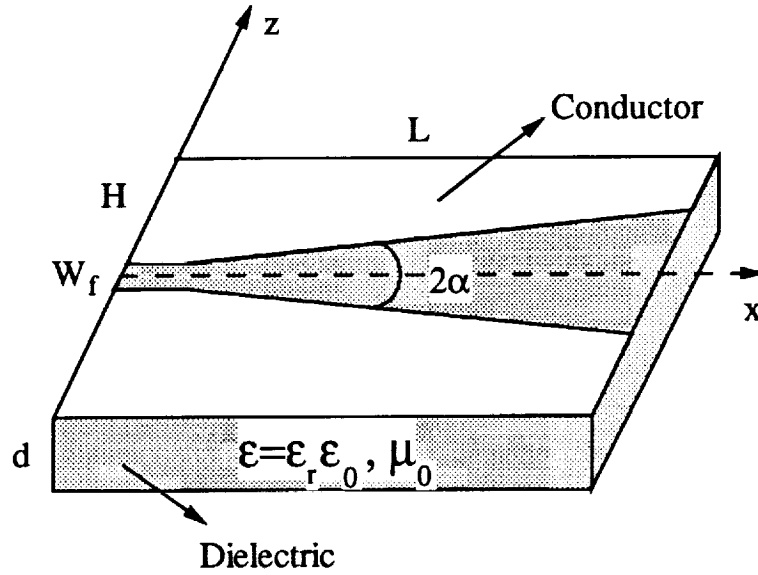


Figure 1.1: LTSA Geometry

The LTSA geometry which is shown in Figure 1.1, does not lend itself to analytical solution with the given parameter ranges. Therefore, a computer modeling scheme and a code are necessary to analyze the problem. This necessity imposes some further objectives or requirements on the solution method (modeling) and tool (computer code). These may be listed as follows:

- A good approximation to the real antenna geometry.
- Feasible computer storage and time requirements.

According to these requirements, the work is concentrated on the development of efficient modeling schemes for these type of problems and on reducing the central processing unit (CPU) time required for the computer code. A Method of Moments (MoM) code is developed for the analysis of LTSA's within the parameter ranges given.

1.2 Significance

An antenna is one of the most important components in all communication systems. With the development of radar during the 1940's, many new antennas have been introduced. The introduction of MoM to electromagnetics made the numerical analysis of many antennas possible. During the 1970's the developments in microstrip devices and circuits vastly increased the possibility of new antenna structures. Planar antennas enjoy the possibility of integration with the other parts of the system. In recent years, the new developments in the millimeter wave frequencies has increased the importance of planar antennas suitable for this frequency range. The tapered slot antenna is one likely candidate for both microwave and millimeter wave systems. It can be easily integrated to microstrip circuits with a microstrip-to-slotline transition. Its radiation characteristics are also promising. Initial studies on LTSA's were mostly

experimental. In recent years, some approximate analytical and numerical solutions for LTSA's have been developed, however the validity of the results are restricted by the choices of the antenna parameters or by the approximation of the real antenna geometry. Therefore, there is a need for better modeling and characterization of these antennas.

This work concentrates on rigorous computer modeling of single LTSA's with the use of MoM. The real antenna geometry is modeled closely for the first time, both the conducting parts of the antenna and the finite size dielectric region. Earlier modelings lacked accuracy in either modeling the conductor parts (by assuming a different shape of the conductors to ease the analysis), or in modeling the dielectric (by assuming the dielectric support infinite or assuming that it is very thin). The characterization of the LTSA will provide the researchers and designers in the field with better design guidelines in the range of the parameters given before. Also, the solution method is not unique to the problem, the analysis of similar structures may be carried out with a modification of the computer code for the particular problem.

1.3 Background

The Tapered Slot Antenna was introduced by Gibson [1]. He called it the Vivaldi Antenna. Since its introduction, its properties have been studied by many researchers in the field [2]-[12]. The first studies were mostly experimental [2, 3], dealing mostly

with the characterization of the antenna and derivation of some empirical design formulas. The usage of the antenna at millimeter wave frequencies as a feed array element [8], and the integration with the other elements of the system have also been studied [11, 12].

The first theoretical formulation for the radiation pattern of the antenna has been provided by R. Janaswamy [4, 6, 7]. In his work, the height of the LTSA (H in Figure 1.1) was assumed infinite. Assuming also infinitely long antennas, ($L \geq 3\lambda_0$), enabled him to approximate the fields by those of two infinite cones which can be analyzed analytically [13]. However, assuming infinite conducting parts for the antenna leads to incorrect predicted fields if one uses the free-space Green's function in the application of the Schelkunoff's equivalence principle [14]. Due to this reason, he approximated the effect of the finite length of the antenna by assuming a conducting half-space at the end of the antenna, and using the related Green's function.

In the analysis of LTSA's on a dielectric substrate the preceeding assumptions do not lead to an analytical solution due to the presence of the dielectric. Therefore, for this part of the analysis, he approximated the antenna taper step-wise, and solved the eigenvalue problem [15], to determine the aperture field distribution up to a multiplicative constant in each constant slot-line section [7]. Enforcing the power conservation principle for each junction yielded the field distribution which in turn was used to find the fields of the antenna with the same half-space Green's function. This analysis also assumes an infinitely long structure and the effect of the dielectric is

not taken into account when finding the radiated fields using the aperture distribution.

In this early work, it has been found experimentally that the radiation properties of the antenna improve as the antenna height gets smaller [4, 7]. However, the summarized analysis is not suitable for the solution of this problem. It also suffers from the treatment of the dielectric presence. In many applications, [2, 11, 12], the length of the antenna is less than $3\lambda_0$, further restricting the applicability of these results. Therefore, there has been a need to analyze the problem within parameter ranges given in Section 1.

Contemporary to our work, attempts have been made to model the antenna by the MoM [9, 10]. In this work, the antenna has been modeled by the skew-plate geometry shown in Figure 1.2. The shortcoming of this approximation is the assumption of differently shaped conductor edges in the distances comparable to the wavelength. Since the approximated geometry of the antenna has also been utilized in experimental models, good agreement with measurements has been obtained. Our results [16] predict different radiation patterns for the real geometry of the LTSA. Also the effect of the dielectric still needed better consideration, since only low-permittivity (ϵ_r), and very thin dielectric support has been analyzed [10].

In electromagnetic radiation and scattering problems there are two main approaches: Differential equation (DE) modeling and integral equation modeling [17]. Traditionally, DE models are used in bounded problems and IE models are employed

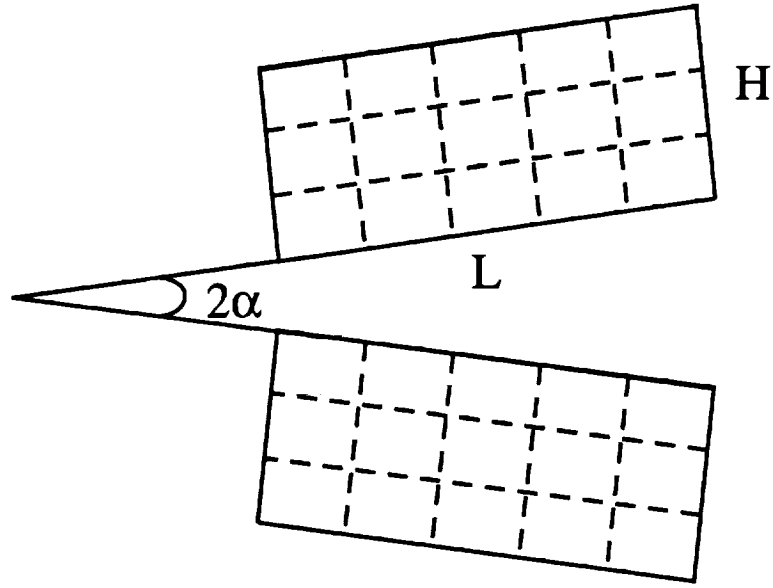


Figure 1.2: Skew-Plate antenna

in exterior radiation and scattering problems. In DE models, the problem region is divided into meshes and the unknown is approximated by a function in each cell. The satisfaction of the boundary conditions at each mesh boundary yields the unknowns related to the fields. In IE models, the integral equation describing the problem is obtained first, then, the unknown in the equation is expanded using some basis functions. Weighting of the IE with some weight functions converts the integral equations to a linear system of equations. Solution for the currents (or unknown in the problem) is obtained by standard matrix inversion or iterative techniques. By their nature, DE models are local and IE models are global, and as a result, the matrices obtained from DE models are large but sparse as opposed to the relatively small and dense matrices obtained from IE models. DE models are extended to radiation and scatter-

ing problems in unbounded regions by utilizing the “absorbative boundary conditions” [18]. However, since large matrices are obtained using DE models and since the solution times are on the same order for both of the methods, we have preferred the IE modeling scheme and MoM formulation [19, 20].

In IE methods, another recent approach is the Conjugate Gradient Method [21, 22], which has been applied to dielectric scattering, scattering from conducting plates and wire antenna problems. However, it is not applicable to mixed bodies such as the dielectric supported LTSA. It has been applied to LTSA’s in air and infinite arrays of LTSA’s by Catedra et al [23].

1.4 Overview of Report

The report is organized as follows. Chapter 2 presents the formulation of generalized scattering or radiation from a coated dielectric body problem. In Chapter 3, the implementation of the method for the LTSA is explained. The modeling approach for the conducting and the dielectric parts of the antenna with the basis and test function choices for MoM formulation is given in this chapter. Possible excitation types for the antenna and the modeling of the source are also discussed in Chapter 3. In Chapter 4, the results and discussion are presented. In section 4.2, favorable comparison to available data in the literature and to experimental measurements is made to verify the computational results. The accuracy of the results is checked and

discussed. A parametric study of air LTSA's with changing L , H and α is given in section 4.3. Conclusions on the behavior of the radiation characteristics of the antenna with respect to these parameters are drawn. In section 4.4, the effect of the dielectric thickness and the permittivity on the radiation characteristics of the antenna are presented. The developed MoM code is explained briefly in Chapter 5. The performance study of the code is also given in this chapter. Finally, the conclusions and the suggestions for future research are presented in Chapter 6.

CHAPTER 2

FORMULATION OF THE METHOD

2.1 Introduction

Many important electromagnetic problems involve radiation and scattering from a dielectric body partially covered with a conductor. This general problem geometry is shown in Figure 2.1. In this figure, the problem is shown as a scattering problem where

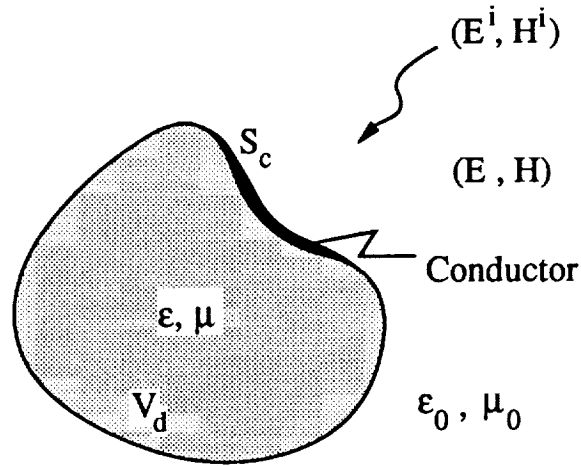


Figure 2.1: Scattering Problem Geometry

$(\mathbf{E}^i, \mathbf{H}^i)$ is the incident field and (\mathbf{E}, \mathbf{H}) , the total field in the presence of the scatterer, is the unknown. The location of the source for $(\mathbf{E}^i, \mathbf{H}^i)$ is assumed to be at infinity so

that $(\mathbf{E}^i, \mathbf{H}^i)$ is not effected by the presence of the scatterer. In radiation problems the same formulation as for the scattering case can be used with only a proper change of the interpretation of the incident field. In this type of problem, $(\mathbf{E}^i, \mathbf{H}^i)$ is the field of the source $(\mathbf{J}_i, \mathbf{M}_i)$ which is usually on or in the structure and assumed to be known or approximated. When attempting to solve the problem numerically, a suitable source model is chosen. As a result of this modeling, some parts of the source model should also be included as having unknown current distribution. This is the major difference of the radiation and scattering cases.

Whether it is a scattering or a radiation problem, the analytical solution of the total fields for Figure 2.1 is very difficult in most cases. When the geometry of the dielectric body is a canonical one such as a sphere or a slab extending to infinity, the specific Green's function can be derived in the frequency domain or a series representation of it may be obtained. However, the solution for the conductor parts of the structure is still very difficult and is usually carried out by a numerical approach [24] such as MoM. For example, when the dielectric body is a slab extending to infinity, the Green's function is easy to derive in the frequency domain [24]. However, in the solution of the unknown conductor currents by moment method, one encounters Sommerfeld integrals which are difficult to integrate numerically. When using series form for the Green's function, the slow convergence is a typical problem.

When the difficulties regarding the Green's function are considered and when the geometry of the particular problem does not allow these approaches, the only possible

way is to use numerical methods [17].

In order to solve the general problem of Figure 2.1 numerically, the governing integral equations for the conductor and dielectric regions are obtained. This is explained in section 2.2. These equations are then solved numerically using MoM. This procedure is detailed in section 2.3. In the remaining sections of this chapter, the dielectric body will be assumed to have the permeability, μ_0 , of free-space, which is the case for most antenna problems.

2.2 Derivation of the Integral Equations

Referring to Figure 2.1, the conducting parts of the structure, S_c , can be modeled by applying Schelkunoff's equivalence [14] principle. According to this principle, the total tangential fields determine the equivalent electric and magnetic surface current densities,

$$\mathbf{J}_s = \mathbf{n} \times \mathbf{H} \quad (2.1)$$

$$\begin{aligned} \mathbf{M}_s &= - \mathbf{n} \times \mathbf{E} \\ &= 0 \end{aligned} \quad (2.2)$$

which are introduced on the surfaces of the conductor; both bottom and top. Here, \mathbf{n} is the unit outward normal to the conducting body. \mathbf{M}_s is equated to zero in (2.2) since a perfect conductor assumption is made and on a perfect conductor the

tangential electric field is zero. When \mathbf{J}_s and \mathbf{M}_s are introduced on the conductor, the conductor can be removed and the currents \mathbf{J}_s , \mathbf{M}_s can be considered to radiate in free-space [25]. If the conductor is very thin, equivalent currents \mathbf{J}_s and \mathbf{M}_s might be considered as the vector sum of the currents on the top and bottom surfaces. Throughout the analysis this assumption will be made for the conductor regions.

In the dielectric region, V_d , Maxwell's equations may be written as:

$$\nabla \times \mathbf{E} = -j\omega\mu_0\mathbf{H} \quad (2.3)$$

$$\begin{aligned} \nabla \times \mathbf{H} &= j\omega\epsilon\mathbf{E} \\ &= j\omega\epsilon_0\mathbf{E} + j\omega(\epsilon - \epsilon_0)\mathbf{E} \end{aligned} \quad (2.4)$$

Subsequently, (2.4) can be rewritten as,

$$\nabla \times \mathbf{H} = j\omega\epsilon_0\mathbf{E} + \mathbf{J}_e \quad (2.5)$$

where

$$\mathbf{J}_e = j\omega(\epsilon - \epsilon_0)\mathbf{E} \quad (2.6)$$

Equation (2.5) can be interpreted as a Maxwell's equation in free-space with a current source \mathbf{J}_e located at the position of the dielectric part of the structure. Therefore, one can replace the dielectric region with the equivalent volume electric polarization current density \mathbf{J}_e and consider the whole problem in free-space [20, 26, 27, 28, 29]. The equivalent problem is shown in Figure 2.2.

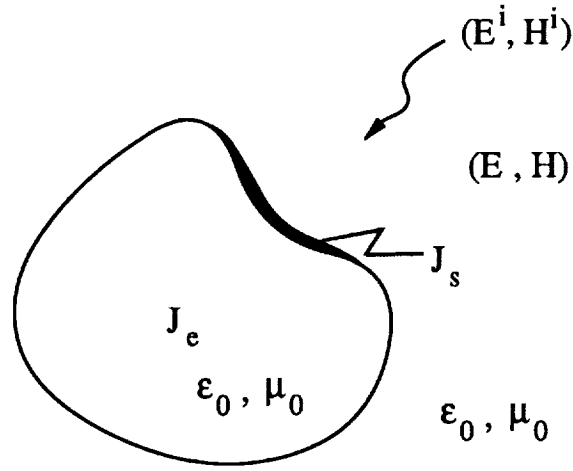


Figure 2.2: Equivalent Problem

On the conductor regions, the total tangential electric field intensity is zero. Therefore, the following equation must be satisfied on the conductor surfaces.

$$(\mathbf{E}^i + \mathbf{E}^s + \mathbf{E}^e)_{tan} = 0 \quad (2.7)$$

In equation (2.7), \mathbf{E}^i , \mathbf{E}^s , and \mathbf{E}^e are the fields radiated by the sources \mathbf{J}_i , \mathbf{J}_s , and \mathbf{J}_e , respectively.

In the dielectric region, V_d , the condition

$$\begin{aligned} \mathbf{E}^s + \mathbf{E}^i + \mathbf{E}^e &= \mathbf{E} \\ &= \frac{\mathbf{J}_e}{j\omega(\epsilon - \epsilon_0)} \end{aligned} \quad (2.8)$$

should be satisfied.

Equation (2.8) is merely the statement of the equality of the total fields in which (2.6) has been used to obtain the relation with the equivalent polarization current density, \mathbf{J}_e , in the dielectric region.

All the fields produced by the equivalent sources and the source can be expressed in terms of the free-space dyadic Green's function as

$$\mathbf{E} = \int_V \mathbf{J} \cdot \overline{\overline{\mathbf{G}}} dV \quad (2.9)$$

where,

$$\overline{\overline{\mathbf{G}}} = (\overline{\overline{\mathbf{I}}} + \frac{1}{k_0^2} \nabla \nabla) g_0 \quad (2.10)$$

and,

$$g_0 = \frac{\exp(-jk_0 R)}{R}. \quad (2.11)$$

$\overline{\overline{\mathbf{I}}}$ is the unit dyad, R is the distance between the source and the field points, $R = |\mathbf{r} - \mathbf{r}'|$, where \mathbf{r} and \mathbf{r}' are position vectors to the field and source points, respectively, and k_0 is the free-space wavenumber. The ∇ operator operates on unprimed coordinates which are the field coordinates. For surface current densities, equations (2.9) through (2.11) still can be used with surface integrals over source current densities replacing the volume integrals.

As a result, equations (2.7) and (2.8) are the two integral equations that must be satisfied by the unknown conductor current density \mathbf{J}_s , and the equivalent volume polarization current density \mathbf{J}_e .

Equation (2.7) states that the total tangential electric field intensity on a conductor surface is zero. Therefore, if a test source \mathbf{J}_m is placed in the conductor, its reaction [25] with all other sources, $(\mathbf{J}_i, \mathbf{J}_s, \mathbf{J}_e)$, will be zero. In equation form this

can be written as:

$$\begin{aligned} \int_{S_e} \mathbf{J}_s \cdot \mathbf{E}^m dS + \int_{S_i} \mathbf{J}_i \cdot \mathbf{E}^m dS + \int_{V_d} \mathbf{J}_e \cdot \mathbf{E}^m dV &= \\ \int_{S_m} \mathbf{J}_m \cdot \mathbf{E}^s dS + \int_{S_m} \mathbf{J}_m \cdot \mathbf{E}^i dS + \int_{S_m} \mathbf{J}_m \cdot \mathbf{E}^e dS &= 0 \end{aligned} \quad (2.12)$$

where S_i and S_m are the regions in which \mathbf{J}_i and \mathbf{J}_m are nonzero. The field \mathbf{E}^m is the field radiated by \mathbf{J}_m in free-space.

Equation (2.12) is a reaction integral equation for the two unknown current densities \mathbf{J}_s and \mathbf{J}_e . Satisfaction of this equation ensures that these currents have the proper reaction with a test source on the conductor surface. However, this does not insure the satisfaction of the field equality equation, (2.8), in the dielectric region. In order to incorporate the effect of the dielectric, we will multiply (2.8) by a vector weighting function \mathbf{W}_m , and integrate over V_d , to obtain,

$$\int_{V_d} (\mathbf{E}^s + \mathbf{E}^e - \frac{\mathbf{J}_e}{j\omega(\epsilon - \epsilon_0)}) \cdot \mathbf{W}_m dV = - \int_{V_d} \mathbf{E}^i \cdot \mathbf{W}_m dV \quad (2.13)$$

Let us rewrite equations (2.12) and (2.13) as:

$$\begin{aligned} \int_{S_e} \mathbf{J}_s \cdot \mathbf{E}^m + \int_{V_d} \mathbf{J}_e \cdot \mathbf{E}^m &= - \int_{S_i} \mathbf{J}_i \cdot \mathbf{E}^m \\ &= -V_m \end{aligned} \quad (2.14)$$

$$\begin{aligned} \int_{V_d} (\mathbf{E}^s + \mathbf{E}^e - \frac{\mathbf{J}_e}{j\omega(\epsilon - \epsilon_0)}) \cdot \mathbf{W}_m dV &= - \int_{V_d} \mathbf{E}^i \cdot \mathbf{W}_m dV \\ &= -V_{m'} \end{aligned} \quad (2.15)$$

Equations (2.14) and (2.15) contain the unknown current densities in their kernels and are the governing reaction integral equations for the problem of Figure 2.1. These two coupled integral equations must be solved to find the unknown conductor and dielectric polarization current densities \mathbf{J}_s and \mathbf{J}_e , respectively. The equations (2.14) and (2.15) must hold for any arbitrary test function \mathbf{J}_m and \mathbf{W}_m . However, in order to solve these equations numerically with MoM, N distinct \mathbf{J}_m and M distinct \mathbf{W}_m will be used to reduce the equations to a square matrix equation, where N and M are the number of expansion functions for the conductor and dielectric regions, respectively.

It is worthwhile to mention here that, although the reaction concept is utilized to obtain (2.14), it is essentially an inner product of the integral equation (2.7) by the test functions \mathbf{J}_m similar to the dielectric equation (2.8) and its inner product (2.15).

2.3 Solution of the Integral Equations by the Method of Moments

In order to solve equation (2.14) and (2.15) by MoM, the unknown currents are expanded as follows:

$$\mathbf{J}_s = \sum_{n=1}^N I_{sn} \mathbf{J}_{sn} \quad (2.16)$$

$$\mathbf{J}_e = \sum_{n=N+1}^{N+M} I_{en} \mathbf{J}_{en} \quad (2.17)$$

The total conductor surface current \mathbf{J}_s is expanded by using the basis functions

\mathbf{J}_{sn} . In the dielectric, the volume polarization current density is similarly expanded using the basis functions \mathbf{J}_{en} . In (2.16) and (2.17) \mathbf{J}_{sn} and \mathbf{J}_{en} have known forms and I_{sn} and I_{en} are the unknown multiplicative constants to be determined. In general, since the conductor current is a surface current density, \mathbf{J}_{sn} should contain two orthogonal components, whereas \mathbf{J}_{en} is a volume current density and should contain three.

Substituting (2.16) and (2.17) into (2.14) and changing the order of integration and summation gives,

$$\begin{aligned} \sum_{n=1}^N I_{sn} \left(\int_{S_c} \mathbf{J}_{sn} \cdot \mathbf{E}^m dS \right) + \sum_{n=N+1}^{N+M} I_{en} \left(\int_{V_d} \mathbf{J}_{en} \cdot \mathbf{E}^m dV \right) &= -V_m \\ &= - \int_{S_i} \mathbf{J}_i \cdot \mathbf{E}^m dS \end{aligned} \quad (2.18)$$

In (2.18), since $\mathbf{J}_{sn}, \mathbf{J}_{en}$ and \mathbf{E}^m are known, the integrals may be evaluated leaving a linear equation in $N + M$ unknowns. Since \mathbf{E}^m is the field of the test sources which are placed on the conductor, using N test sources in (2.18) gives N equations in $N + M$ unknowns.

Similarly, when (2.16) and (2.17) are substituted into (2.15) we obtain,

$$\begin{aligned} \sum_{n=1}^N I_{sn} \left(\int_{V_d} \mathbf{E}^{sn} \cdot \mathbf{W}_m dV \right) + \\ \sum_{n=N+1}^{N+M} I_{en} \left(\int_{V_d} \left(\mathbf{E}^{en} - \frac{\mathbf{J}_{en}}{j\omega(\epsilon - \epsilon_0)} \right) \cdot \mathbf{W}_m dV \right) &= -V_m' \\ &= - \int_{V_d} \mathbf{E}^i \cdot \mathbf{W}_m dV \end{aligned} \quad (2.19)$$

where \mathbf{E}^m and \mathbf{E}^{en} are the fields produced by the surface and the volumetric basis functions (currents), \mathbf{J}_m and \mathbf{J}_{en} , respectively. When M weighting functions are used in (2.19), M equations in $N + M$ unknowns result. Together with those obtained from (2.18) a square matrix of order $N + M$ is obtained.

Equations (2.18) and (2.19) represent a linear system of equations which can be written compactly,

$$\sum_{n=1}^{N+M} I_n Z_{mn} = V_m \quad \text{for } m = 1, \dots, N + M \quad (2.20)$$

or in the matrix form as,

$$\mathbf{Z}\mathbf{I} = \mathbf{V} \quad (2.21)$$

where, \mathbf{Z} is the square impedance matrix, \mathbf{I} is the current vector, and \mathbf{V} is the excitation or voltage vector, and,

$$I_n = \begin{cases} I_m & \text{if } n = 1, \dots, N \\ I_{en} & \text{if } n = N + 1, \dots, N + M \end{cases} \quad (2.22)$$

$$V_m = \begin{cases} -\int_{S_i} \mathbf{J}_i \cdot \mathbf{E}^m dV & \text{if } m = 1, \dots, N \\ -\int_{V_d} \mathbf{E}^i \cdot \mathbf{W}_m dV & \text{if } m = N + 1, \dots, N + M \end{cases} \quad (2.23)$$

After the matrix elements, z_{ij} , are calculated using numerical integration, the unknown current coefficients are solved by standard inversion or iteration procedures.

Until this point the method is general in the sense that, neither the basis functions for the conductor and the dielectric, nor the testing (weighting) functions for them

are specified. The difficulty or the complexity of the matrix element evaluation and the computation time for them are heavily influenced by these choices. The chosen basis and testing functions and their impact on the implementation of the method for LTSA's will be explained in the next chapter.

CHAPTER 3

IMPLEMENTATION OF THE METHOD FOR LINEARLY TAPERED SLOT ANTENNA

3.1 Introduction

In this chapter, the implementation of the method explained in chapter 2 will be given. In order to apply the formulation of the previous chapter to the antenna geometry of Figure 3.1, the conducting parts of the antenna should be approximated by a surface modeling scheme. The definitions of the unknown currents on the conducting surfaces

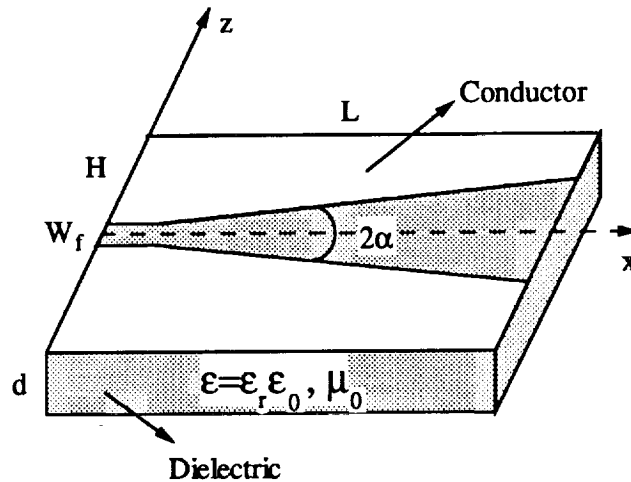


Figure 3.1: LTSA Geometry

will complete this part of the analysis. The next step is to approximate the dielectric geometry and define the unknown currents for the dielectric region. When the test functions for both the conducting and the dielectric parts are determined, the matrix elements can be calculated.

The approximation of the conducting and dielectric parts also involves the modeling of the source. Depending on the source modeling, unknowns related to the source may be included in the matrix equation.

After the matrix equation is obtained by calculating the matrix elements and the right-hand side vector, the solution of this equation gives the unknowns. Once the unknown currents are calculated, any necessary information of the antenna such as the far-field radiation pattern, field distribution in the dielectric, input impedance, can be calculated easily.

3.2 Conductor Modeling

Possible choices for modeling the conductor surfaces are triangular sectioning [30, 31], polygonal plate modeling [32, 33, 34], or a combination of these with rectangular sectioning [35, 36]. As mentioned in chapter 2, the complexity of the matrix element calculation depends on this choice. Although triangular and polygonal plate modeling schemes are better in conformity to the surface than rectangular sectioning, the number of integrations involved in calculating the matrix elements is larger. Triangular

sectioning is best suited for modeling the LTSA geometry, however the integrations in the matrix element calculations have to be carried out on a triangular domain which is costly and difficult to do numerically. Polygonal plate sectioning is also suited to modeling the LTSA geometry. The difficulty in matrix element calculation however is worse than both the triangular and rectangular sections. The matrix element calculation integrations are four-fold in this case. Rectangular sectioning gives the simplest expressions for the matrix elements and is the least costly in terms of the computation time. Hence, whenever applicable, rectangular sectioning offers simplicity and computational savings. Referring to Figure 3.1, the range of the taper angle for useful antennas was determined earlier [4] to be less than 9 degrees. This small taper angle allows a good approximation with the unequally sized rectangular segmentation of Figure 3.2.

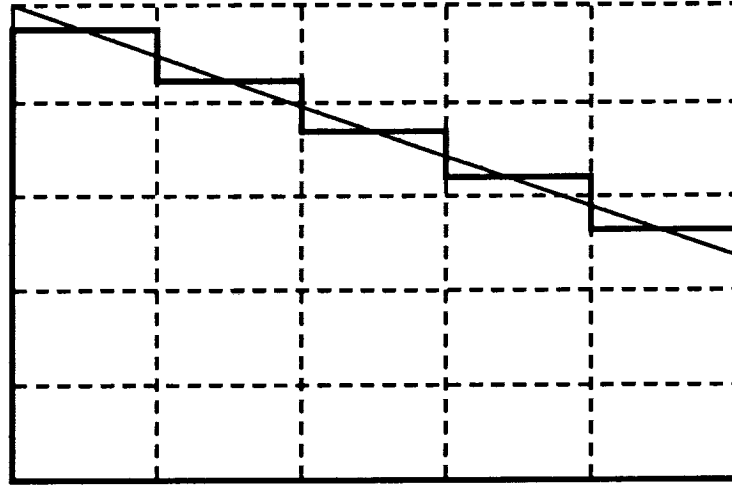


Figure 3.2: Unequal Size Rectangular Sectioning

3.3 Conductor Basis and Test Functions

The conductor current basis functions are chosen as overlapping piecewise sinusoidal functions. The current on the i th segment of the conductor consists of two monopoles. The current starts on the segment i and extends to the next segment. Each segment carries a monopole current which has components J_{z_i} and J_{x_i} defined by,

$$J_{z_i} = \mathbf{a}_z \frac{1}{2w_i} \left\{ \frac{I_{1i} \sin[k_0(h_i - z_i)] + I_{2i} \sin(k_0 z_i)}{\sin(k_0 h_i)} \right\} \quad (3.1)$$

$$J_{x_i} = \mathbf{a}_x \frac{1}{h_{i+1}} \left\{ \frac{I_{1i} \sin[k_0(w_i - x_i)] + I_{2i} \sin[k_0(w_i + x_i)]}{\sin(2k_0 w_2)} \right\} \quad (3.2)$$

where \mathbf{a}_z and \mathbf{a}_x are the unit vectors in the directions of z and x , respectively, $2w_i$ is the segment width, and h_i is the segment height. I_{1i} and I_{2i} are the terminal currents, and take the values either 0 or 1. z_i and x_i are the local coordinate variables of the monopole measured from the bottom and the center of the monopole, respectively (See Figures 3.4 and 3.5). The x component of the monopole current extends h_{i+1} along z , to provide current overlap for the successive unequal-size rectangular sections. These monopole currents are piecewise sinusoidal in the current direction and constant transverse to it, and are the same as those in [25].

The combination of the two neighboring segment currents creates one unknown for the conductor. This combination and the resulting current distribution is shown in Figure 3.3. As seen from Figure 3.3, the conductor currents are continuous in the current direction since every surface dipole current overlaps a neighboring one.

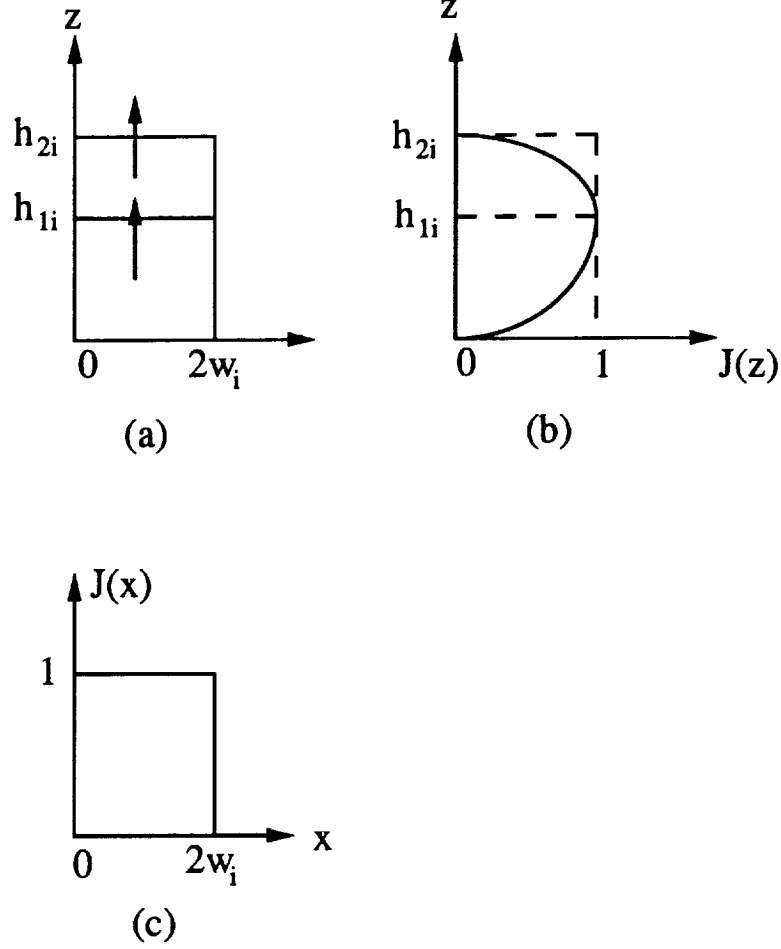


Figure 3.3: Piecewise Sinusoidal Conductor Currents a) Segment geometry b) Distribution in Current Direction c) Distribution in Perpendicular Direction

The current is a constant with respect to the coordinate perpendicular to the current direction. The continuity of the current is a desired property for two reasons. Firstly, the current on the conductor is continuous, therefore, using continuous basis functions allows a good approximation, especially where the current is rapidly varying. Secondly, a discontinuous current approximation creates line charges where the current is discontinuous. Since this would be a fictitious line charge that shouldn't

be present it might lead to erroneous results for antenna currents and therefore other calculated results.

The test functions to complete the application of (2.18) are chosen the same as the basis functions. This is called Galerkin formulation. For this specific choice of basis and test functions, the matrix elements for the conductor-conductor interactions become mutual impedances between the respective currents. These mutual impedances are obtained by summing up the four monopole-to-monopole mutual impedances [25]. With the rectangular sectioning and the defined current distributions, there are only two types of monopole-to-monopole mutual impedance calculations. These are parallel and perpendicular cases which are shown in Figure 3.4 and Figure 3.5. With this choice of rectangular sectioning and current definition the monopole-to-monopole mutual impedances of Figure 3.4 and Figure 3.5 were earlier calculated by integrating the mutual impedance of line currents [36, 37, 38, 39] over the monopole surfaces. The simplest formula for the parallel case is reported in [40]. For the perpendicular case, a one dimensional integral formula for the mutual impedance between a dipole and a monopole is reported in [41]. None of these earlier formulations is valid for unequally sized parallel or perpendicular monopole-to-monopole interactions. The direct integration for the surface currents leads to faster and easier evaluation of matrix elements even in the general case of unequal size segments. Simple formulas for the mutual impedances of the two cases shown in Figure 3.4 and Figure 3.5 have been derived and reported in [42]. The derivations and the resulting expressions will

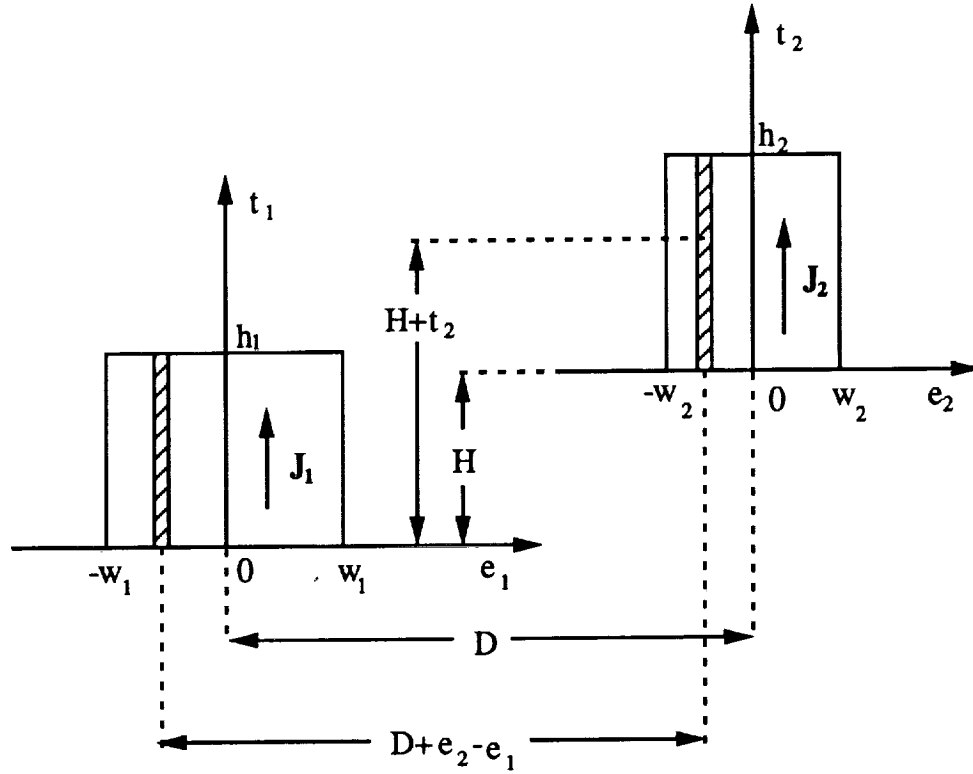


Figure 3.4: Parallel Monopoles

not be repeated here, however, it is worthwhile to mention that the parallel case contains only one-dimensional integrals and the perpendicular case is in closed form, containing exponential integrals only. It is these simple formulas that led to the choice of unequal size rectangular sectioning of the conductor. Tremendous savings of computation time makes possible the use of finer grid sizes and therefore better approximations of the antenna geometry. Another resulting benefit of the rectangular sectioning is the increased symmetry that further reduces the computation time. In large method of moment calculations it is important to consider the symmetries and eliminate the unnecessary computations. In summary, compared to triangular

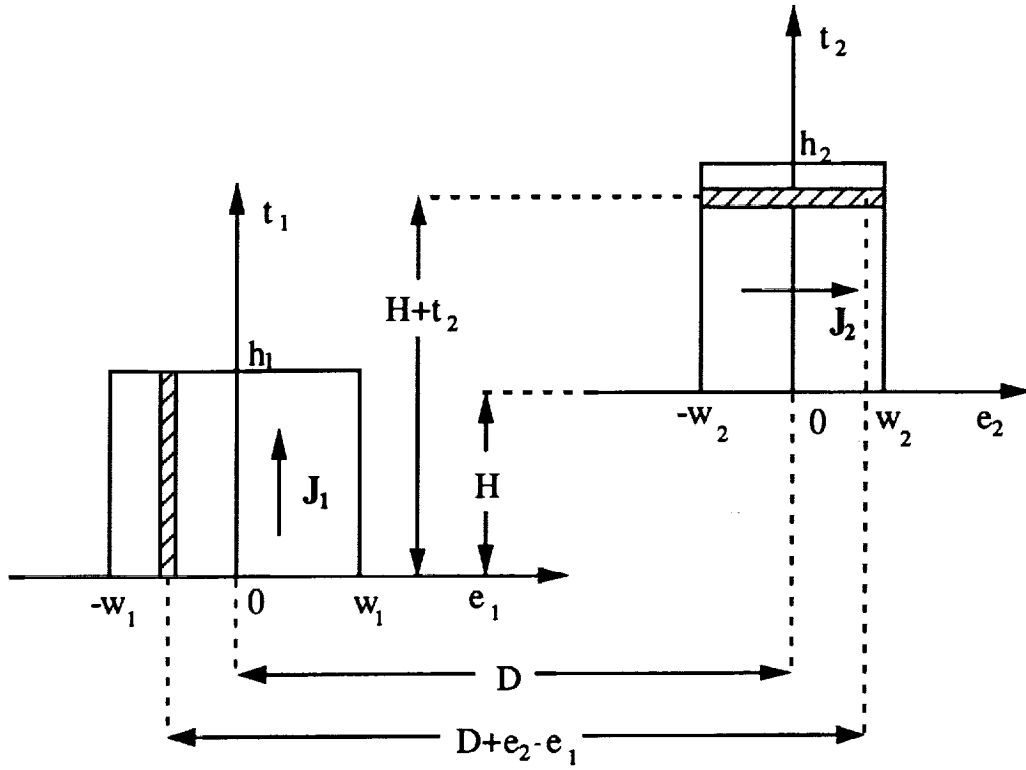


Figure 3.5: Perpendicular Monopoles

and polygonal plate modeling, rectangular sectioning is more efficient for the LTSA geometry.

3.4 Dielectric Modeling

The dielectric region of the LTSA of Figure 3.1 is a rectangular slab with a thickness d . Therefore, any sectioning scheme would easily conform to its geometry. The most common modeling technique for the slab geometry that has extensively been used in the earlier work is cubical sections [26, 27, 28, 29]. For arbitrary dielectric shapes,

tetrahedron modeling has been employed [43] . Since cubical sectioning has been successfully used in the modeling of similar antenna structures, it has been employed in this work (See Figure 3.6).

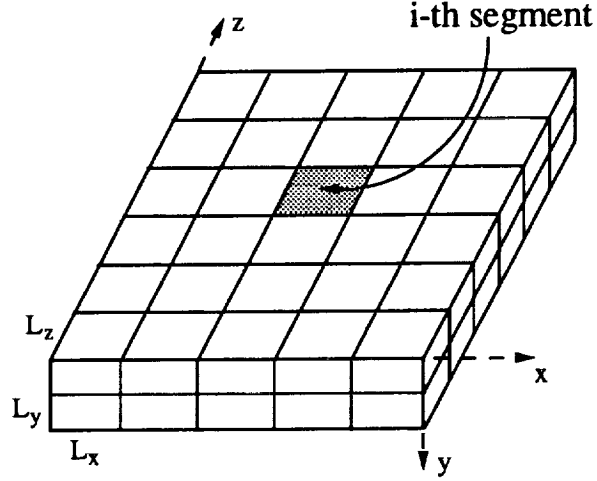


Figure 3.6: Dielectric Segmentation

3.5 Dielectric Basis and Test Functions

In the dielectric region, pulse basis functions are employed which are suitable for the segmentation of Figure 3.6. Therefore, the polarization current density in the dielectric region is expanded as

$$\mathbf{J}_{ei}(x, y, z) = \frac{\alpha_i}{L_y L_z} \mathbf{a}_x + \frac{\beta_i}{L_x L_z} \mathbf{a}_y + \frac{\gamma_i}{L_x L_y} \mathbf{a}_z \quad (3.3)$$

if (x, y, z) is in the i -th cell , (Figure 3.6), and zero if outside.

In the analysis of microstrip antennas, the assumption of infinite dielectric is

usually employed [44, 45, 46]. Since the finite dimensions of the dielectric are ignored in this assumption and since Sommerfeld-type integral evaluations are necessary for the calculation of the matrix elements, this approach is unsuitable for the LTSA analysis. In the analysis of scattering by homogeneous dielectrics, surface current formulations have also been employed [47, 48], which is also applicable to the LTSA problem. However, the case study for a sample LTSA has revealed that the surface current formulation would lead to larger matrix sizes and more difficult numerical integrations for the matrix element computations compared to the volumetric pulse expansion given in equation (3.3). The simplicity of volumetric pulse functions in terms of integration complexity was also the reason why overlapping triangular or sinusoidal basis functions were not preferred.

The expansion of the dielectric volume polarization current density by (3.3) satisfies the criteria that the divergence of the electric field intensity inside a homogeneous dielectric region is zero [29]. However, it introduces surface polarization charges on the faces of the volumetric pulses. The effect of these surface charges has been found to be negligible for the LTSA modeling.

The same modeling scheme for the dielectric regions has been successfully applied to dielectric scattering problems and wire antenna problems [28]. Recently, it has also been applied to the analysis of microstrip antennas [29].

The test functions for the dielectric region are chosen as delta functions located

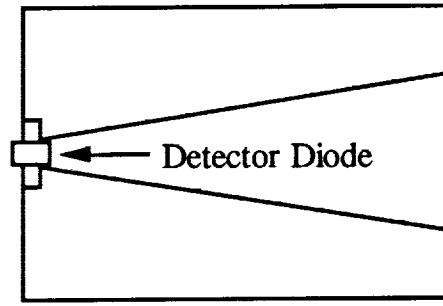
at the center of each cell and directed in \mathbf{a}_x , \mathbf{a}_y and \mathbf{a}_z directions. When employed in (2.19), this test function choice results in the field equation (2.8), which is merely a statement of the equality of the total fields at the center of each dielectric segment and for each component of the electric field intensity in \mathbf{a}_x , \mathbf{a}_y and \mathbf{a}_z directions.

The reason for the choice of this test function is basically its simplicity. Other test functions would introduce additional complexity in addition to already numerically difficult field calculation for three dimensional sources, especially in the source region itself [49].

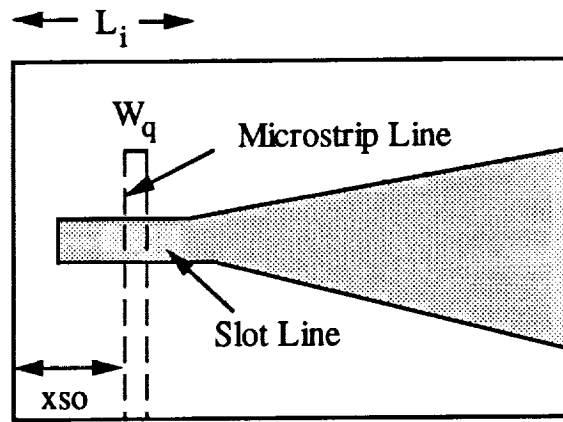
3.6 Source Modeling

Good source modeling in the LTSA analysis is very important because of the fact that the source can contribute to the radiation pattern appreciably. The reason for the source contribution is the openness of the feeding structures. The source region of the LTSA may differ appreciably according to the mode in which the antenna is being used or according to the feeding structure that is employed. Two of the most commonly used source configurations are shown in Figure 3.7. When the antenna is used in the receiving mode, power can be picked up easily by a detector diode soldered across the apex of the antenna as shown in part a) of Figure 3.7

The second source configuration employs a microstripline-to-slotline transition [50] as shown in part b) of Figure 3.7. In this figure, L_i is the input transition



(a)



(b)

Figure 3.7: Possible Source Configurations of the LTSA a) Receiving mode with a detector diode b) LTSA with a microstripline to slotline transition

length, x_{s0} is the distance of the microstripline to the antenna edge and W_q is the width of the microstripline. In this configuration power is delivered to the slotline with a microstripline which extends $\lambda_{ms}/4$ past the slotline edge, where λ_{ms} is the microstrip wavelength. Slotline, on the other hand, is short-circuited $\lambda_{sl}/4$ away from the microstripline edge, λ_{sl} being the slotline wavelength. This configuration creates a resonant structure with a very good voltage standing wave ratio over narrow

bandwidths [50]. The bandwidth can be increased by using matching circuitry on the microstripline, while impedance matching the latter to the other parts of the circuit at the same time.

Different source configurations of the LTSA must be modeled differently. For the diode reception mode, the diode is modeled as a dipole with a delta gap generator at its center [20]. When the dipole thickness is made equal to the thickness of the detector diode, it has been shown earlier that this source modeling yields good results [10].

For the input configuration of Figure 3.7, the microstrip radiation is initially modeled by an infinitesimal current element at the center of the slotline and the other parts of the antenna are approximated by rectangular sectioning, including the short circuit for the slot line. This has been accomplished by introducing another current at the exact short circuit location. The length of the short circuit current is made greater than the slot line width so as to make the current flow between the lower and upper parts of the antenna. It is found that the current element modeling for the microstripline gives very satisfactory results for the co-polar radiation characteristics of the antenna. However, it cannot predict the correct level of cross polarized radiation in the boresight direction. Therefore, a third source model is developed which accounts for the microstripline rigorously, by defining currents on the microstrip as well. The feed point of the microstrip is approximated by a current element in y direction, which avoids the difficulty of introducing the connection mode

currents between the microstripline and the antenna plates. This third model is found satisfactory for determining the radiation characteristics of the antenna, as will be seen in Chapter 4.

3.7 Evaluation of the Matrix Equation

The choices of the conductor and dielectric basis and test functions of sections 3.3 and 3.5 determine how the matrix elements will be computed. Assuming N unknowns for the conducting parts and S segments for the dielectric region, there will be $3S$ unknowns in the dielectric. Therefore, $3S = M$ of (2.19). If we consider Z as,

$$Z = \begin{bmatrix} A_{N \times N} & B_{N \times M} \\ C_{M \times N} & D_{M \times M} \end{bmatrix} \quad (3.4)$$

A and **B** submatrices will have elements which are calculated by reaction integrals.

For currents J_i and J_j the reaction integral is given by

$$\begin{aligned} Z_{ij} &= \int_{S_j} \mathbf{E}^i \cdot \mathbf{J}_j dS \\ &= \int_{S_i} \mathbf{E}^j \cdot \mathbf{J}_i dS \end{aligned} \quad (3.5)$$

where \mathbf{E}^i and \mathbf{E}^j are the fields radiated by J_i and J_j , respectively, and S_i and S_j are the regions where J_i and J_j are nonzero. Submatrix **A** consists of the conductor-conductor interactions. Its elements are calculated by the reaction integrals between the conductor currents only. The calculation of these elements is explained in Section

3.3 since it is related to the geometry approximation directly. These elements are calculated by using the expressions reported in [42].

Since delta functions are chosen as the testing functions in the dielectric region, **C** and **D** submatrices are comprised of the fields radiated by the conductor currents and the dielectric polarization currents respectively at the center of each segment. Evaluation of the **C** submatrix elements is carried out using field equations for piecewise sinusoidal line sources [14]. The field of any conductor current can be found by adding the fields of the corresponding monopoles that makes up the whole current. Referring to Figure 3.1, conductor currents can be in x or z directions only. For a current in z direction, the components of the electric field intensity, Z_{CD_s} , where s stands for x , y or z component, can be found as

$$Z_{CD_x} = \sum_{i=1}^2 C_i \sum_{m=1}^2 \int_{-k_0 \omega_i}^{k_0 \omega_i} \alpha_m \frac{(k_0 D - x)(k_0 L + \beta_m)}{[(k_0 D - x)^2 + (k_0 H)^2]} \frac{\exp(-jR_m)}{R_m} \quad (3.6)$$

$$Z_{CD_y} = \sum_{i=1}^2 C_i \sum_{m=1}^2 \int_{-k_0 \omega_i}^{k_0 \omega_i} \alpha_m \frac{k_0 H(k_0 L + \beta_m)}{[(k_0 D - x)^2 + (k_0 H)^2]} \frac{\exp(-jR_m)}{R_m} \quad (3.7)$$

$$Z_{CD_z} = \sum_{i=1}^2 -C_i \sum_{m=1}^2 \int_{-k_0 \omega_i}^{k_0 \omega_i} \alpha_m \frac{\exp(-jR_m)}{R_m} \quad (3.8)$$

where D , H and L are the distances between the center point of the monopole i and the center of the dielectric cell, in x , y and z directions, respectively, as shown in Figure 3.8. The various other parameters are

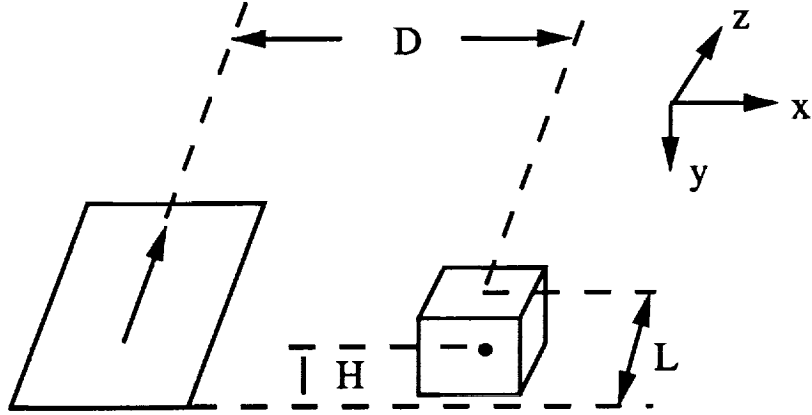


Figure 3.8: Geometry of conductor and dielectric currents

$$C_i = \frac{-j30k_0}{2k_0\omega_i \sin(k_0 h_i)}$$

$$\alpha_1 = I_{2i} \cos(k_0 h_i) - I_{1i}$$

$$\alpha_2 = I_{2i} - I_{1i} \cos(k_0 h_i)$$

$$\beta_1 = -k_0 h_i$$

$$\beta_2 = 0$$

$$R_m = [(k_0 L + \beta_m)^2 + (k_0 D - x)^2 + (k_0 H)^2]^{1/2} .$$

The fields of the x -directed currents can be found using equations (3.6-3.8) with a coordinate rotation.

Returning to the submatrix **B**, and considering that its elements are the reaction integrals between the conductor currents and the dielectric currents, the following approach is applied in their calculation. The dielectric cell is divided into smaller cubical sections and the fields of the conductor current is calculated at the center of

each small section. Multiplication of these fields with the volume of the subdivision and summation over the cell gives a good approximation to the elements of the **B** submatrix. Therefore, if the dielectric cell has dimensions L_x , L_y and L_z and if it is divided into n_x , n_y and n_z segments in x , y and z directions, respectively, the reaction, Z_{DC} , of a z directed conductor current on a dielectric current becomes

$$Z_{DC_s} = \sum_{i=1}^{n_x} \sum_{j=1}^{n_y} \sum_{k=1}^{n_z} -Z_{CD_{ijk}} J_{e_s} \frac{L_x L_y L_z}{n_x n_y n_z} \quad (3.9)$$

where $Z_{CD_{ijk}}$ is the field of the conductor current at the center of the subdivision ijk , and s represents x , y or z directed dielectric current. The interactions between the x -directed conductor and dielectric currents can be found by using (3.9) with a coordinate rotation for the conductor current. This approximation to the dielectric-conductor interaction submatrix **B** is justified because of the fact that MoM usually yields diagonally dominant impedance matrices. Since the elements of **B** are off-diagonal, the results will not be as sensitive to errors in the calculation of these elements compared to the ones in diagonal elements of **A** and **B**.

The elements of the submatrix **D** are directly calculated using equations (2.9-2.11). When calculating the field of a cell current in itself, the singularity in the expression is extracted as suggested in [49]. For the off-diagonal elements of **D**, the same type of approximation as (3.9) is made to reduce the computation time.

The voltage vector calculation also follows the same approach. The first N elements are the reactions of the source and the conductor expansion currents, the

remaining $M = 3S$ are the fields radiated by the assumed source distribution at the center of the dielectric segments.

All of the numerical integrations for the evaluation of the matrix elements are carried out using Gauss-Chebyshev quadratures which are suitable for oscillatory kernels.

3.8 Solution of the Matrix Equation

The matrix equation,

$$\mathbf{Z}\mathbf{I} = \mathbf{V} \quad (3.10)$$

is solved by using the Conjugate Gradient (CG) method [51, 52, 53]. CG method is an iterative conjugate direction method. In Conjugate Direction method the error functional is minimized successively in the directions of a set of \mathbf{Z} -orthogonal vectors. A set of vectors \mathbf{P}_n , $n = 1, 2, \dots, (N + M)$ is said to be \mathbf{Z} -orthogonal (or \mathbf{Z} -conjugate) if they satisfy

$$\langle \mathbf{Z}\mathbf{P}_i, \mathbf{P}_j^* \rangle = 0 \quad \text{for } i \neq j \quad (3.11)$$

where $*$ denotes the conjugate.

In conjugate direction methods, at each iteration, $\mathbf{I}_n + \alpha_n \mathbf{P}_n$ is minimized where \mathbf{P}_n lies on the $(N + M - 1)$ dimensional hyperplane

$$\langle \mathbf{P}_n^*, \mathbf{Z}\mathbf{I} - \mathbf{V} \rangle = 0 \quad (3.12)$$

whose normal is ZP . The conjugate direction methods differ in the way P_n are obtained. When the vectors P_n are obtained by Z -orthogonalization of the residual vectors, R_n , which will be defined subsequently, a CG method results.

The CG method is applicable to Hermitian matrices (operators). In the dielectric supported LTSA case the matrix Z is not symmetric and hence, CG method cannot be applied to (3.10) directly [51]. In order to satisfy the symmetry and the positive definite requirements for Z , both sides of (3.10) can be multiplied by Z^T , where T denotes transpose conjugate. The CG algorithm can then be applied to the transformed equation without actually forming the product $Z^T Z$ [54].

For an initial guess I_0 , the CG method starts by evaluating,

$$\begin{aligned} R_0 &= V - ZI_0 \\ P_0 &= Z^T R_0 \end{aligned} \tag{3.13}$$

and then develops each successive approximation by,

$$I_{n+1} = I_n + \alpha_n P_n \tag{3.14}$$

where

$$\alpha_n = \frac{\|Z^T R_n\|^2}{\|Z P_n\|^2} . \tag{3.15}$$

The residual vectors are generated as

$$R_{n+1} = R_n - \alpha_n Z P_n . \tag{3.16}$$

The direction vectors at each iteration are obtained as

$$\mathbf{P}_{n+1} = \mathbf{Z}^T \mathbf{R}_{n+1} + \beta_n \mathbf{P}_n \quad (3.17)$$

where

$$\beta_n = \frac{\|\mathbf{Z}^T \mathbf{R}_{n+1}\|^2}{\|\mathbf{Z}^T \mathbf{R}_n\|^2}. \quad (3.18)$$

This algorithm minimizes the norm of the residual, $\|\mathbf{R}_n\|$, at each iteration. The iterations are terminated when the error norm, $\|\mathbf{R}_n\|$ is less than some ratio of the initial error norm, $\|\mathbf{R}_0\|$. The initial guess in this work is taken as zero vector in all computed results. Therefore, $\|\mathbf{R}_0\| = V$. When $\|\mathbf{R}_n\| \leq 10^{-4} \|\mathbf{R}_0\|$, the iterations are terminated. Different tolerance values (10^{-5} , 10^{-6}) have also been employed to check the sensitivity of the results around the solution with the same input data. The solutions obtained with smaller tolerances are nearly identical in terms of the radiation pattern and current distribution, and hence, 10^{-4} is used in further results.

CG method has many nice features that make it useful in the solution of large linear systems of equations such as the one obtained in the LTSA analysis. Some of these which might explain the preference of CG iteration over the direct methods can be outlined as [54, 55]:

- The method is highly insensitive to the initial guess \mathbf{I}_0 . As mentioned earlier, $\mathbf{I}_0 = 0$ is chosen in all of the computations involved in this work, with no difficulty in obtaining the solution.

- The number of iterations required for CG method is equal to the number of distinct eigenvalues of the matrix \mathbf{Z} [54]. This property makes CG method especially useful for large MoM applications, since in most of the cases, the eigenvalues of \mathbf{Z} are closely spaced. Actually, it is this property that favors CG method over direct methods since CG method lowers its computational cost with closely spaced eigenvalues. In order for CG method to be less costly compared to Gaussian Elimination, the number of iterations should be less than $(N+M)/3$, where $(N+M)$ is the size of the matrix \mathbf{Z} . Most of the results in this work are obtained with number of iterations less than this number.
- The convergence of CG method is $1/K$ quadratic [54], assuming that the solution is reached in K iterations. The reason for this rate definition of Sarkar [54] is that the algorithm requires K steps to achieve the effect of one step of a method with a true quadratic convergence rate.

CHAPTER 4

RESULTS AND DISCUSSION

4.1 Introduction

In this chapter, the results of the analysis of LTSA's in air or with a dielectric support will be given. Verification of the computed results and comparison to experimental measurements are given section 4.2. A parametric study of air LTSA's is explained in Section 4.3. Finally, the computed results for dielectric LTSA's are presented in Section 4.4, where the effect of the dielectric thickness and permittivity are investigated.

The radiation patterns of the antenna in the E -Plane, H -Plane and the D -Plane are used throughout this chapter. With the coordinate system of Figure 3.1 for the antenna configuration, E -Plane of the antenna coincides with the $x - z$ Plane, whereas H -Plane is the $x - y$ plane, as shown in Figure 4.1 and Figure 4.2, respectively. The D -Plane is a diagonal plane located at 45 degrees to the E and H -Planes. The radiated patterns are measured and computed for co-polar and cross-polar components. The co-polar component of the field of the antenna is the θ component for both principal

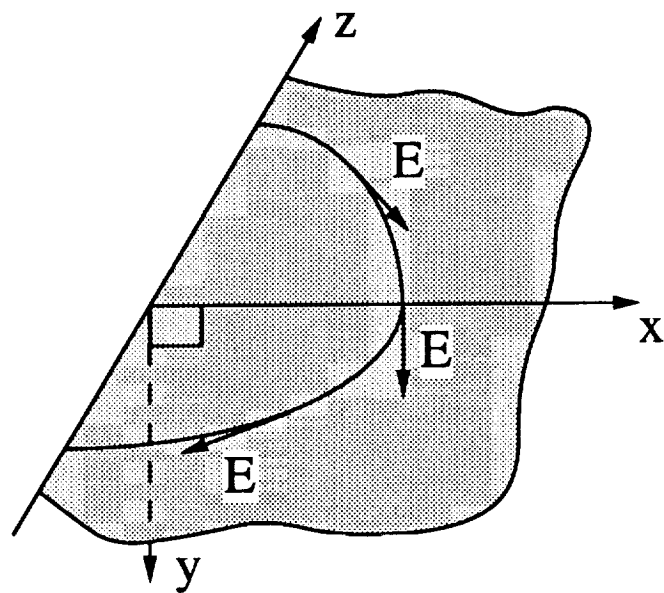


Figure 4.1: E-Plane of the LTSA

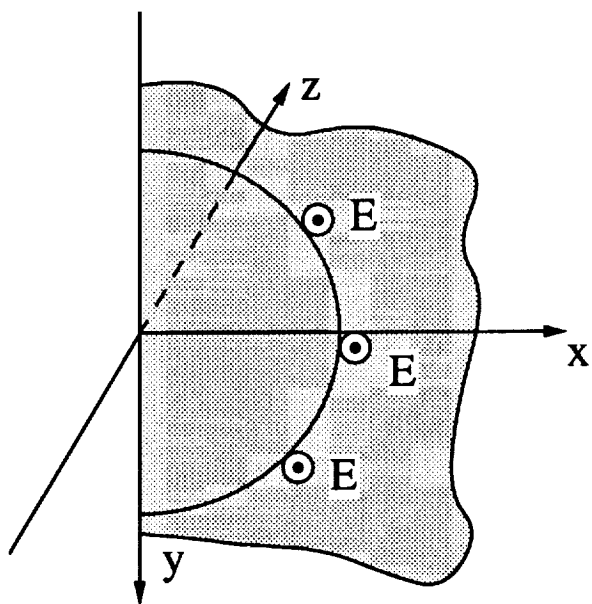


Figure 4.2: H-Plane of the LTSA

planes (E and H). Therefore, E and H plane data are measured by considering Figure 4.1 and Figure 4.2, and measuring the field component in the direction shown by the direction of \mathbf{E} in the mentioned figures. In the E-Plane, $\phi = 0$ degrees and θ is varying, whereas in the H-Plane, $\theta = 90$ degrees and ϕ is varying. These can be better understood by considering Figure 4.3 which shows the LTSA and the standard gain antenna positioning. In Figure 4.3 it is assumed that the test antenna (LTSA) is used in receive mode and the polarization of the transmit antenna is as shown, however, everything remains for the transmit mode operation of the LTSA. Considering Figure 4.3, co-polar measurements can be listed as:

- E-Plane: $\beta_r = 90$ degrees, $\beta_t = 90$ degrees.
- H-Plane: $\beta_r = 0$ degrees, $\beta_t = 0$ degrees.
- D-Plane: $\beta_r = 45$ degrees, $\beta_t = 45$ degrees.

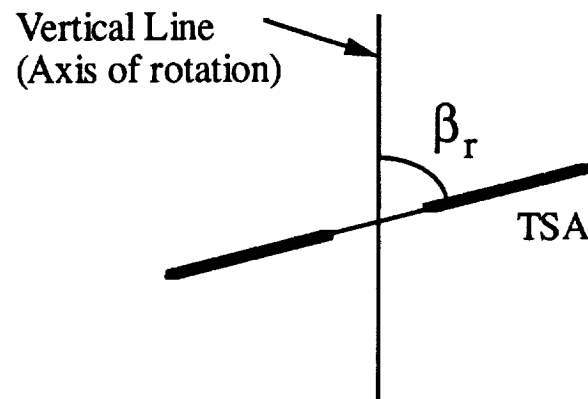
For cross-polar measurements, changing the polarization of the transmit antenna will be sufficient, which means changing β_t . This measurement strategy for the cross-polarized fields conforms to the third definition of Ludwig [56]. Therefore, cross-polar measurements can be done with the following set-up.

- E-Plane: $\beta_r = 90$ degrees, $\beta_t = 0$ degrees.
- H-Plane: $\beta_r = 0$ degrees, $\beta_t = 90$ degrees.

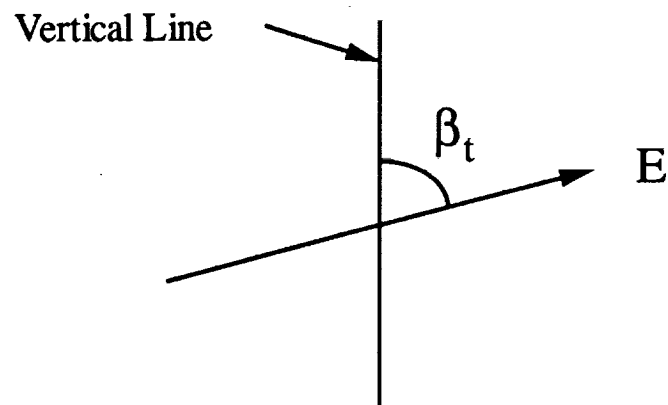
- D-Plane: $\beta_r = 45$ degrees, $\beta_t = -45$ degrees.

4.2 Verification of Computed Results

Numerical results obtained using the code are tested and verified both computationally and experimentally. First, the unequal-size rectangular sectioning scheme of section 3.2 is tested. In order to do this, the analysis is extended to handle all four edges of the skew-plate antenna of Figure 1.2. The results of this analysis is compared to those obtained from another code which uses skew segments, and hence models the skew-plate antenna exactly in the geometrical sense. In many cases that are computed, very good agreement is observed between the results. Figures 4.4 and 4.5 show the comparison for the *E*-Plane and *H*-Plane co-polar radiation patterns, respectively, for a skew-plate antenna with $L = \lambda_0$, $H = 0.5\lambda_0$, $\alpha = 5$ deg and $W_f = 0.004\lambda_0$. In the skew segmentation model, 7 segments across the length and 4 segments across the height are used. In the rectangular model, the number of divisions are 8 for the length and 5 for the height. As can be seen from Figures 4.4 and 4.5, the two computations agree very well, the largest difference between the two being about 1 dB. Considering that all four sides are approximated with unequal-size rectangular modeling and the fact that there is only one edge in the actual LTSA geometry, which is approximated in this manner, it is concluded that the accuracy would be even better in that case.



(a)



(b)

Figure 4.3: Antenna configurations a) LTSA positioning, b) Standard gain antenna positioning.

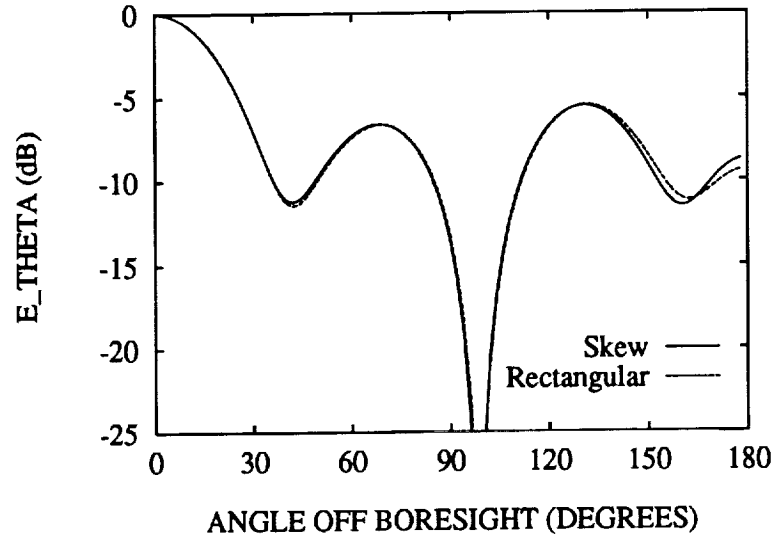


Figure 4.4: Comparison of E-Plane radiation patterns for skew-plate and unequal-size rectangular modeling ($L = 1.0\lambda_0$, $H = 0.5\lambda_0$, $W_f = 0.004\lambda_0$, $\alpha = 5$ degrees).

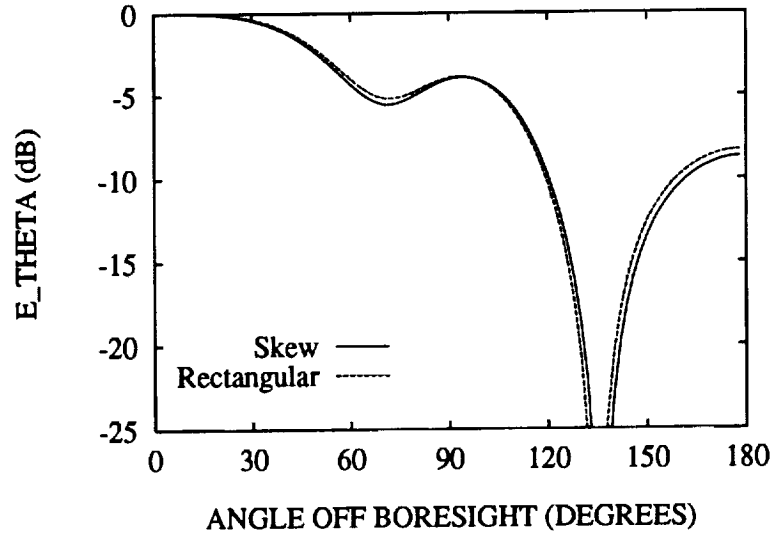


Figure 4.5: Comparison of H-Plane radiation patterns for skew-plate and unequal-size rectangular modeling ($L = 1.0\lambda_0$, $H = 0.5\lambda_0$, $W_f = 0.004\lambda_0$, $\alpha = 5$ degrees).

The convergence of the unequal size rectangular sectioning model is usually obtained using 6 to 7 segments per wavelength across the length and 4 to 5 segments per wavelength across the height of the LTSA. The number of segments required across the length is larger because the unequal-size rectangular sectioning is more sensitive to segmentation across the length. Figures 4.6 and 4.7 show the radiation pattern comparison for two different segmentations in the E and H planes, respectively, of a skew-plate antenna with parameters $L = 5.2\lambda_0$, $H = 0.9\lambda_0$, $W_f = 0.06\lambda_0$ and $\alpha = 7$ deg. The data represented by solid lines in these figures are obtained by

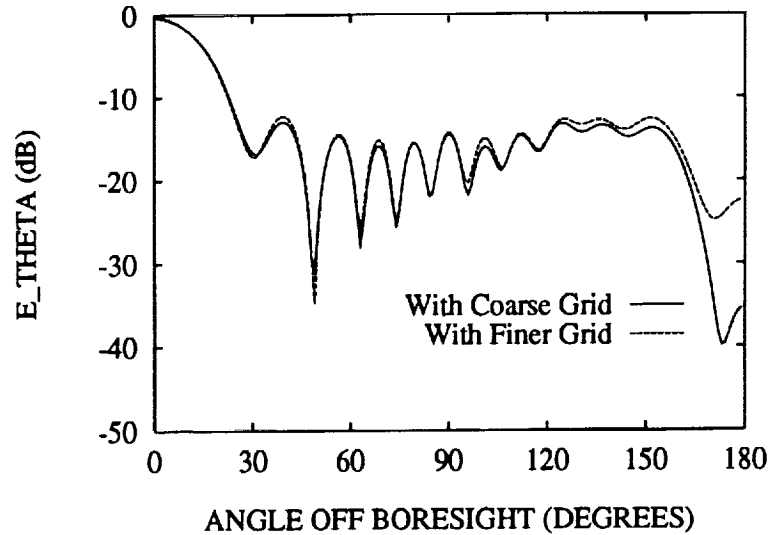


Figure 4.6: E-Plane radiation pattern for a skew-plate antenna with two different segmentation ($L = 5.2\lambda_0$, $H = 0.9\lambda_0$, $W_f = 0.06\lambda_0$, $\alpha = 7$ degrees).

using 30 segments across the length and 6 segments across the height, whereas the dotted lines are obtained using 35 and 7 segments across the length and the height,

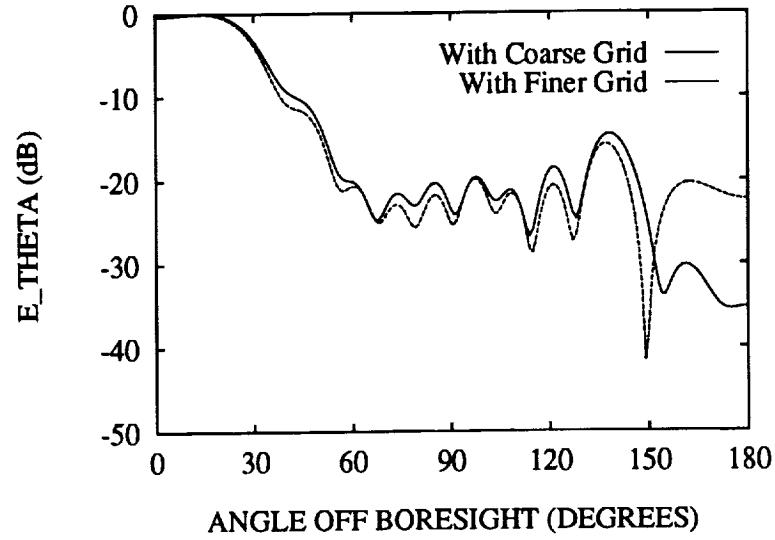


Figure 4.7: H-Plane radiation pattern for a skew-plate antenna with two different segmentation ($L = 5.2\lambda_0$, $H = 0.9\lambda_0$, $W_f = 0.06\lambda_0$, $\alpha = 7$ degrees).

respectively. As can be seen from the figures, the analysis results are very close to each other until 150 degrees. The effect of the difference in segmentation is observed only after 150 degrees, displaying the good convergence behavior of the algorithm. The parameters of this antenna are chosen the same as that analyzed in [10, 5]. The results of Figures 4.6 and 4.7 agree very well with those reported in [10].

The ultimate test on any electromagnetic modeling code is done by calculating the near fields at the conducting boundary and in the dielectric region and checking the calculations for the satisfaction of the boundary conditions [17]. The cost of this test is the same as the solution of the MoM matrix equation and hence is not practical for large problem sizes. However, an easier approach to test the near-field behavior of a code is to calculate the current distribution on/in the structure and check it for

abnormalities in the amplitude and phase. This approach is used in this work to test the near-field performance of the code. Figures 4.8 to 4.11 show the magnitude and phase plots of the current on a LTSA with $L = 5.2\lambda_0$, $H = 1.5\lambda_0$, $W_f = 0.06\lambda_0$ and $\alpha = 7$ deg.

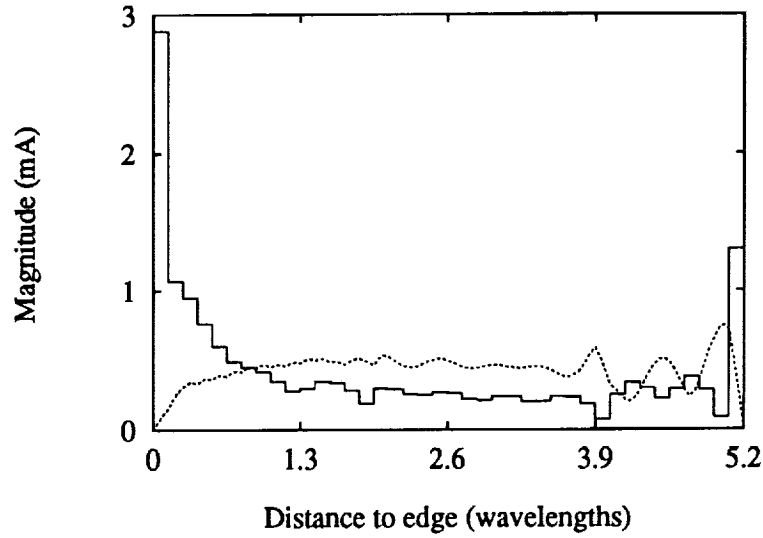


Figure 4.8: Magnitude of antenna current along $z = 0.75\lambda_0$. — : J_x , - - - : J_z .

Figures 4.8 and 4.9 show the magnitude and phase variation of the x and z components of the antenna current along a horizontal (z) cut at $0.75\lambda_0$ away from the lower antenna edge. Figures 4.10 and 4.11 gives the same components for horizontal (x) cut at $2.53\lambda_0$ away from the antenna edge. The traveling wave nature of the z component of the current is evident in Figures 4.8 and 4.9, and both the amplitude and the phase are free of abnormal behavior. The current displays a standing wave

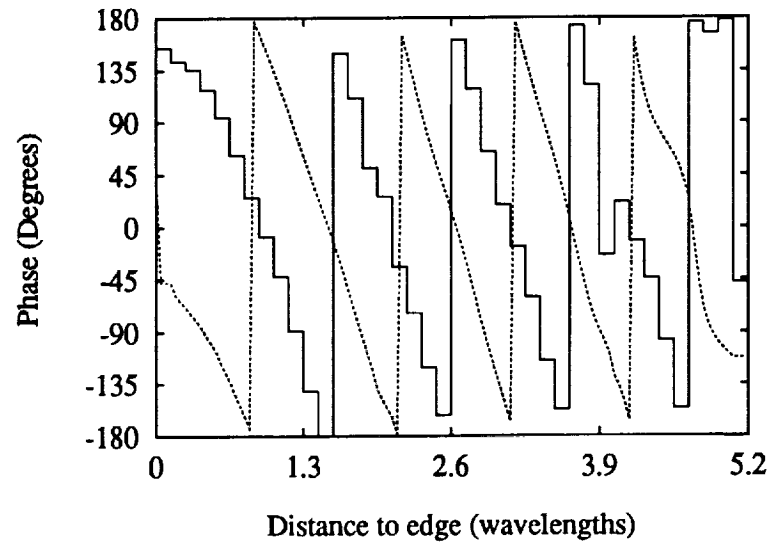


Figure 4.9: Phase of antenna current along $z = 0.75\lambda_0$. — : J_x , - - - : J_z .

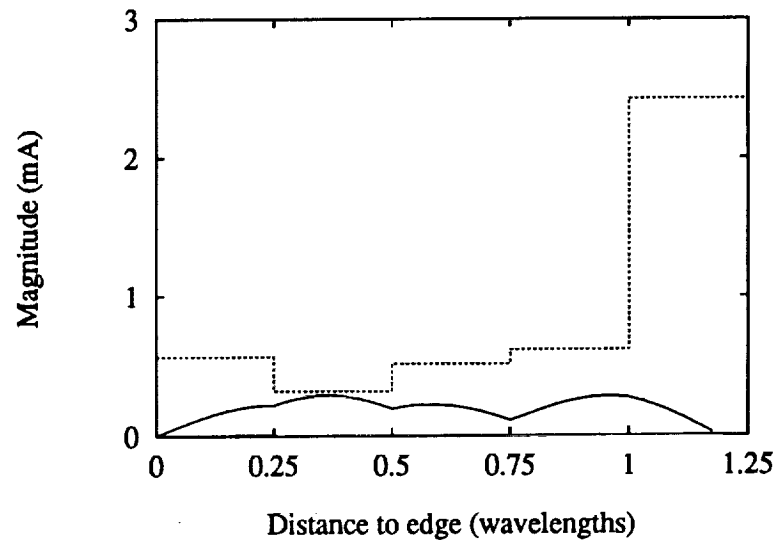


Figure 4.10: Magnitude of antenna current along $x = 2.53\lambda_0$. — : J_x , - - - : J_z .

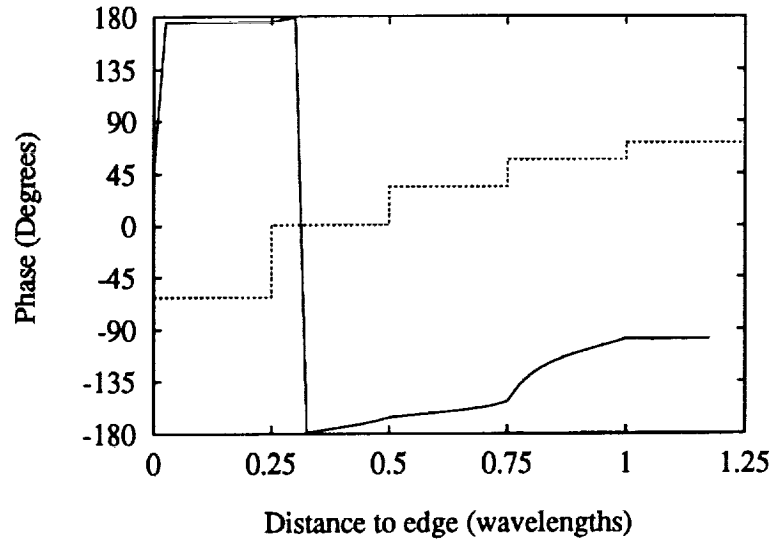


Figure 4.11: Phase of antenna current along $x = 2.53\lambda_0$. — : J_z , - - - : J_x .

nature in z direction, as shown in Figures 4.10 and 4.11. This should be expected because the antenna height is small ($1.5\lambda_0$) and the current bounces back and forth between the two edges of the antenna.

Computed results are also verified by experimentation. For this purpose, two antennas are built and measurements are taken in E , H and D planes. The first antenna is intended to check the air LTSA results and was built using 5-mil brass sheet and supported using styrofoam which has a permittivity (1.05), very close to that of free-space. Microstripline to slotline transition is used in the feeding section of the antenna which extends $0.5\lambda_0$, where λ_0 is the wavelength at the operating frequency of 9 GHz. The feeding part of the antenna is designed using 31-mil, $\epsilon_r = 2.33$, Duroid substrate. The substrate is terminated abruptly at the apex of the antenna, where

the taper starts. The guidelines given in [50] are used to design the microstripline to slotline transition which resulted in slotline impedance of 138.2Ω and microstripline impedance of 120Ω . This slotline impedance is achieved with $W_f = 0.659$ mm ($0.01977\lambda_0$ at 9 GHz). The wavelength in the slotline is 2.88 cm ($0.864\lambda_0$), whereas the microstripline wavelength is 2.4793 cm ($0.74379\lambda_0$). The width of the microstripline for 120Ω characteristic impedance is found as 0.4171 mm ($0.01251\lambda_0$). In order to match the microstripline to the 50Ω output impedance of the test equipment, a quarter wave impedance transformer is designed at the center frequency of 9 GHz. The final design is shown in Figure 4.12, where $H = 1.5\lambda_0$, $L_i = 0.5\lambda_0$, $xs0 = 0.216\lambda_0$, $c = 0.01251\lambda_0$, $d = 0.03392\lambda_0$, $e = 0.0679\lambda_0$, $f = 0.63221\lambda_0$, and $g = 0.45\lambda_0$.

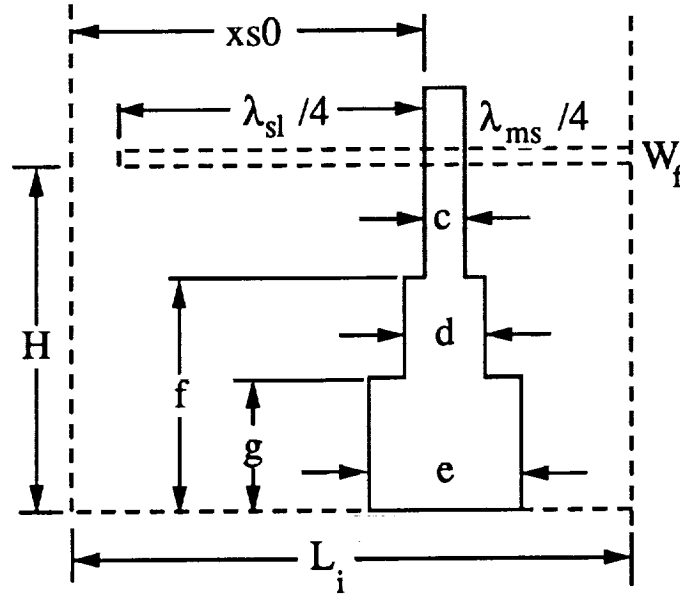


Figure 4.12: Feed design of the test antenna

The comparison between computation and measurement for co-polar E and H plane radiation patterns is given in Figure 4.13. Figure 4.14 shows the comparison for the co-polar and cross-polar radiation patterns in D plane. In the computation the dielectric support at the feeding part of the antenna is modeled rigorously. The microstripline feed is modeled using only 120Ω characteristic impedance line extending to the edge of the antenna. In the numerical model 48 segments across the length and 6 segments across the height of the conductor are used. The microstripline is modeled by 17 segments, resulting in 1059 conductor unknowns. The dielectric segments across length, width, and height are 4, 34 and 1, respectively, which give 408 dielectric current unknowns. The solution time for this case was 2062 CPU seconds on CRAY Y-MP.

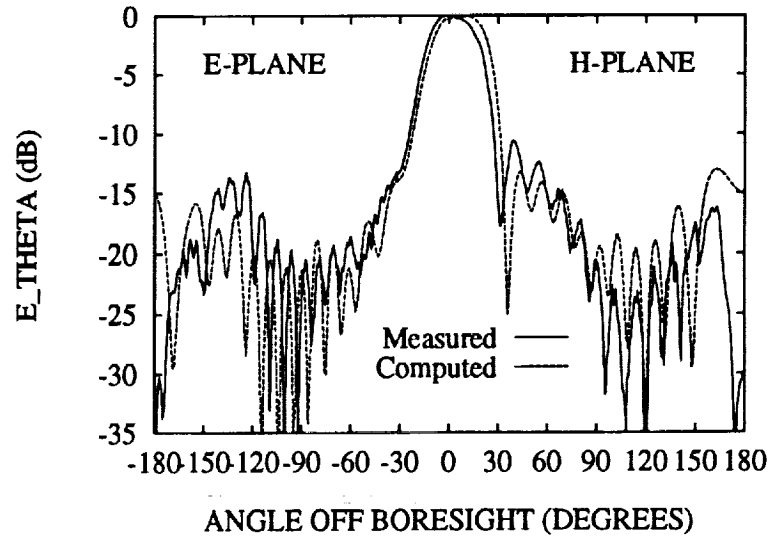


Figure 4.13: Measured and computed co-polar radiation patterns for LTSA in air ($L = 5.5\lambda_0$, $L_i = 0.5\lambda_0$, $H = 1.5\lambda_0$, $W_f = 0.02\lambda_0$, $\alpha = 7$ degrees).

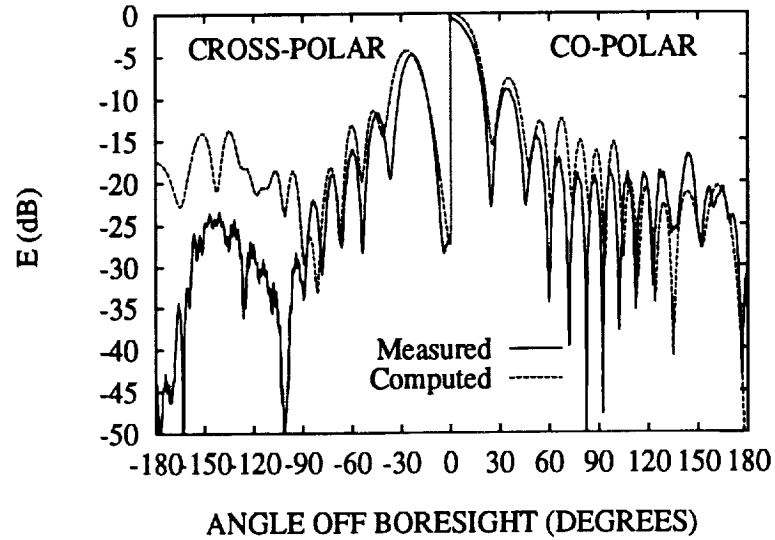


Figure 4.14: Measured and computed co-polar and cross polar D-Plane radiation pattern for LTSA in air ($L = 5.5\lambda_0$, $L_i = 0.5\lambda_0$, $H = 1.5\lambda_0$, $W_f = 0.02\lambda_0$, $\alpha = 7$ degrees).

As can be seen from Figures 4.13 and 4.14, quite good agreement is obtained between the computed results and measured data. The computed pattern predicts the main beam and the first side lobe level correctly. The pattern shapes also agree well. Slight discrepancies between the two is thought to be resulting from the alignment errors during the manufacturing of the test antenna and from the effect of the adhesive used to attach the antenna to the styrofoam. The difference between the cross-polar measured and calculated data below -90 degrees results from the use of an absorber piece over the source region during the measurements. However, the maximum cross polarization level and the cross polarized pattern is predicted correctly by the code until this angle. The effect of the absorber is negligible for the co-polar measurements,

which leads to the good agreement for this part of the comparison.

The second test antenna is built using a 31-mil thick, $\epsilon_r = 2.33$ Duroid substrate, and is used to evaluate the dielectric LTSA calculations. This antenna has the same feed design values as the air LTSA test antenna. Figures 4.15 and 4.16 show the comparison for the E and H plane co-polar radiation patterns and co-polar and cross-polar radiation patterns for the D plane, respectively. The computed patterns for this case is obtained using 36 segments in length and 6 segments in height for the conductor parts, 17 segments for the microstripline, 40 segments in length, 1 segment in height and 24 segments in width for the dielectric region. The total number of unknowns is 3541 of which 661 is the conductor unknowns. The solution time for this case was 2766 CPU seconds on CRAY Y-MP.

A very good agreement is observed between the computed and measured data for this case. The code predicts the shape and the amplitudes of the radiation patterns accurately for this antenna as well. Actually, the agreement is better for this antenna since the dielectric support of the antenna extends through the whole length of the antenna. In the air case test antenna, the dielectric support is terminated in the feed section and hence the diffraction from the dielectric edge can be appreciable and is not handled by the code due to choice of the basis functions in the dielectric. Also, the slight discrepancies after 150 degrees in dielectric LTSA comparisons is again attributed to the use of an absorber block in the measurements over the input section of the antenna which is not modeled by the code.

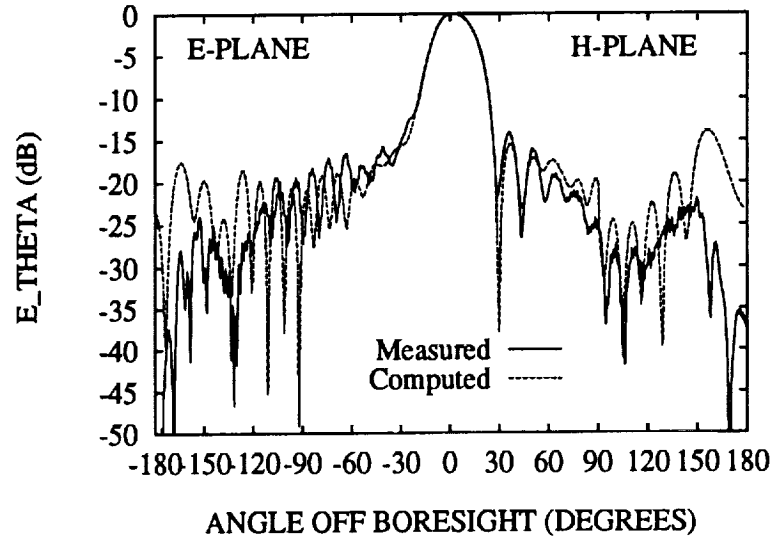


Figure 4.15: Measured and computed co-polar E and H-Plane radiation patterns for a dielectric LTSA ($\epsilon_r = 2.33$, $d = 0.02362\lambda_0$, $L = 5.5\lambda_0$, $L_i = 0.5\lambda_0$, $H = 1.5\lambda_0$, $W_f = 0.02\lambda_0$, $\alpha = 7$ degrees).

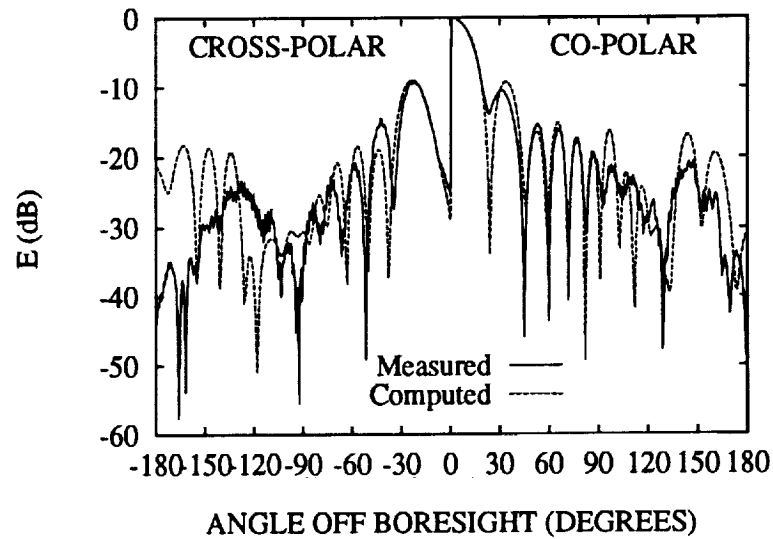


Figure 4.16: Measured and computed co-polar and cross-polar D-Plane radiation patterns for a dielectric LTSA ($\epsilon_r = 2.33$, $d = 0.02362\lambda_0$, $L = 5.5\lambda_0$, $L_i = 0.5\lambda_0$, $H = 1.5\lambda_0$, $W_f = 0.02\lambda_0$, $\alpha = 7$ degrees).

The comparisons with available data in the literature and with experimental data that is presented in this section leads to the conclusion that the theoretical model and the code can predict the radiation characteristics of air or dielectric linearly tapered slot antennas with reasonable accuracy.

4.3 Computed Results for Air Tapered Slot Antennas

In this section, computed results for air LTSA's will be presented. In [4], Janaswamy has observed that as the antenna height is decreased for fixed length and taper angle, better radiation patterns are achievable. In order to address this question, a parametric study of air LTSA's is planned and carried out. Since the behavior of the dielectric LTSA is quite similar to the air LTSA, conclusions drawn for the air LTSA can also be applied to the dielectric LTSA. In the parametric study, the apex width, W_f , of the LTSA is chosen as 2 mm (0.06λ at 9 GHz) and the antennas are assumed to be in the receiving mode with a diode soldered at the apex. The diode is modeled by a strip dipole of width 0.02λ and length 0.2λ . Three levels for each of the parameters L , H and α are chosen. The levels for α are 5 deg, 7 deg and 9 deg. H assumes the values of λ , 1.5λ and 2λ , whereas L varies as λ , 3λ and 5λ . The analysis is valid for any frequency provided that all dimensions are the same used in the analysis in terms of the wavelength. These three levels for α , H and L resulted in 27 numerical experiments. Co-polar radiation patterns in E , H and D planes and

cross-polar radiation patterns in D plane are computed for all experiments. Table 4.1 shows the experiments and the corresponding calculated figures of merit. The figures of merit used in Table 4.1 are:

1. EBW: 3-dB beamwidth in the co-polar E -Plane radiation pattern,
2. ESL: First sidelobe level in the E -Plane radiation pattern,
3. HBW: 3-dB beamwidth in the co-polar H -Plane radiation pattern,
4. HSL: First sidelobe level in the H -Plane radiation pattern,
5. DBW: 3-dB beamwidth in the co-polar D -Plane radiation pattern,
6. DSL: First sidelobe level in the D -Plane radiation pattern,
7. DXL: Peak cross-polarization level in the D -Plane radiation pattern.

Since the antenna and the receiving strip dipole are symmetric about the plane $z = 0$, the cross polarization is theoretically zero ($-\infty dB$), in the E and H planes of the antenna. This fact is also verified in the calculations. Considering Table 4.1, the following observations are made:

- As H decreases for a fixed L and α , EBW first decreases and then starts to increase again. ESL also behaves in the same manner. However, HBW increases steadily whereas HSL decreases. The D -Plane radiation pattern follows the same trend as the E -Plane with first decreasing then increasing DBW and

Table 4.1: Results for the air LTSA study

Exp. No	L	H	α	EBW	ESL	HBW	HSL	DBW	DSL	DXL
1	5	2	9	32.0	-11.41	41.2	-5.81	38.7	-7.66	-2.98
2	5	2	7	34.84	-14.02	41.0	-6.06	40.44	-6.72	-2.28
3	5	2	5	38.72	-15.08	42.0	-6.49	42.58	-5.84	-1.37
4	5	1.5	9	18.6	-14.05	48.4	-10.07	24.86	-9.76	-6.54
5	5	1.5	7	20.0	-14.97	48.36	-10.35	26.28	-8.66	-5.57
6	5	1.5	5	20.84	-12.20	48.52	-10.65	27.2	-7.60	-4.95
7	5	1.0	9	32.9	-11.52	65.0	-20.38	36.24	-6.01	-4.18
8	5	1.0	7	34.5	-15.62	61.84	-19.64	36.36	-5.29	-3.91
9	5	1.0	5	40.9	-13.05	64.64	-20.07	38.96	-4.86	-3.28
* 10	3	2	9	43.2	-12.50	52.2	-5.63	52.1	-7.52	-2.38
* 11	3	2	7	44.0	-11.4	53.12	-5.62	52.40	-6.82	-2.00
* 12	3	2	5	45.0	-9.26	54.2	-5.45	52.62	-6.51	-1.86
13	3	1.5	9	26.0	-4.31	59.24	-6.64	35.74	-5.93	-2.97
14	3	1.5	7	26.5	-4.10	53.96	-7.19	34.1	-6.26	-3.38
15	3	1.5	5	25.12	-3.79	54.0	-7.21	33.0	-5.77	-3.04
16	3	1.0	9	38.2	-12.31	71.22	-17.47	44.2	-5.88	-4.72
17	3	1.0	7	41.6	-10.02	72.2	-18.42	46.1	-4.75	-4.17
18	3	1.0	5	45.3	-7.7	73.4	-17.31	48.0	-3.93	-3.73
** 19	1	2.0	9	101.4	-2.87	87.2	-6.48	72.0	-3.94	0
** 20	1	2.0	7	100.6	-2.48	86.0	-5.79	71.4	-3.67	0
** 21	1	2.0	5	100.0	-2.08	84.6	-5.05	71.0	-3.38	0
** 22	1	1.5	9	95.6	-2.45	98.5	-3.78	94.0	-3.21	0
** 23	1	1.5	7	95.0	-1.99	92.4	-3.20	93.0	-2.92	0
** 24	1	1.5	5	94.0	-1.54	87.0	-2.56	91.6	-2.63	0
** 25	1	1.0	9	81.5	-2.49	80.4	-3.66	96.2	-5.13	0
** 26	1	1.0	7	81.0	-2.03	79.5	-3.25	95.6	-4.76	0
** 27	1	1.0	5	80.4	-1.55	78.8	-2.78	93.8	-4.37	0

DSL. The peak cross polarization level in the D -Plane behaves differently for antennas of different length. For $L = 5\lambda$, DXL first decreases then starts to increase, however, for $L \leq 3\lambda$ it steadily decreases as H decreases. Figures 4.17 and 4.18 display these behaviors. The experiment numbers of Table 4.1 are

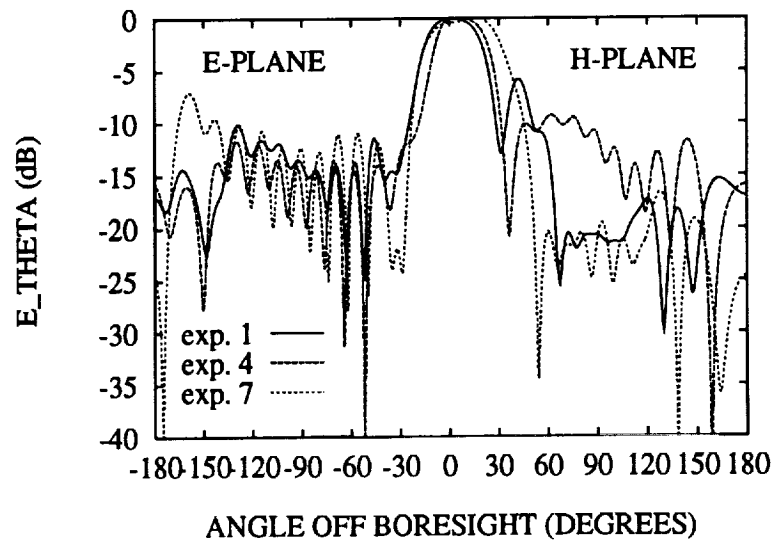


Figure 4.17: Variation of E and H -Plane patterns of LTSA's with H .

used to identify the data in these figures.

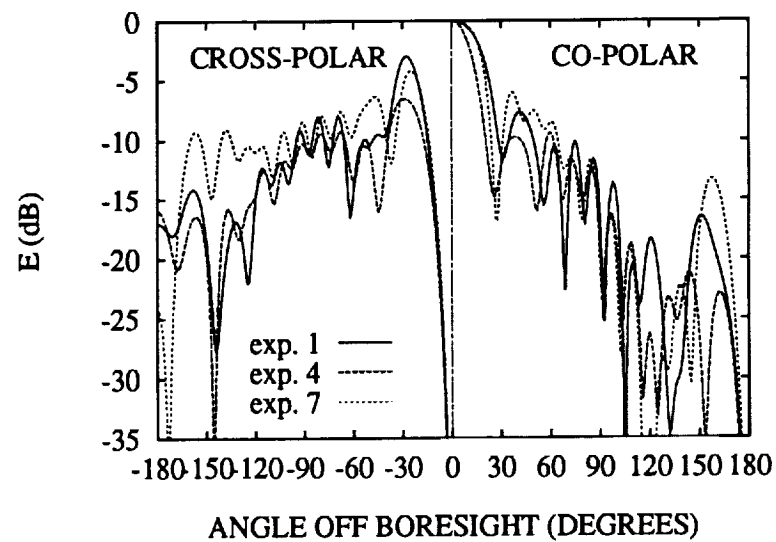


Figure 4.18: Variation of D -Plane pattern of LTSA's with H .

- As α decreases, EBW increases. ESL decreases slightly for $L = 5\lambda$. For shorter antennas, EBW remains nearly the same, however ESL increases. The H -Plane of the antenna is not as sensitive to variation in α , the main beam and sidelobe levels and the shape remain nearly the same, while lobe locations change slightly. Only for $H = \lambda$ and $L = 5\lambda$, a slight decrease of HBW is observed with decreasing α . DBW, DSL and DXL increase with decreasing α , the largest deviation in DXL being for large L . These variations are shown in Figures 4.19 and 4.20.

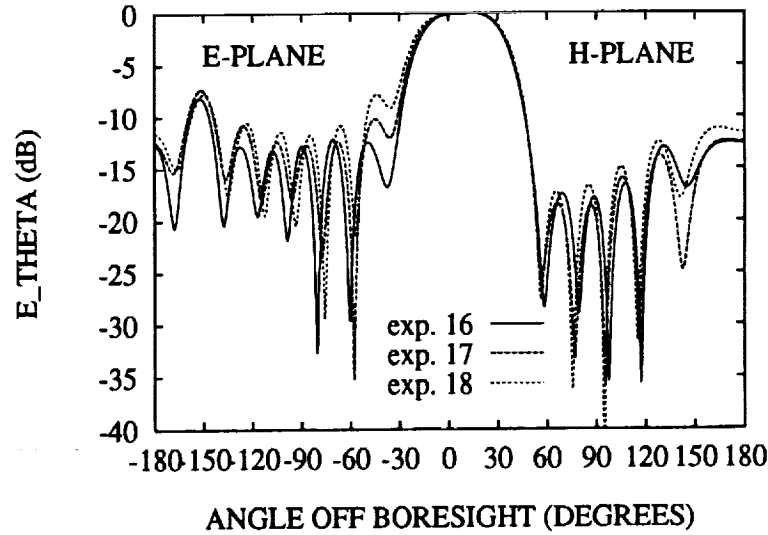


Figure 4.19: Variation of E and H -Plane patterns of LTSA's with α .

- As L increases, the antenna behaves as expected. All of the 3 dB beamwidths decrease, with decreasing sidelobe levels and peak cross polarization level in D -

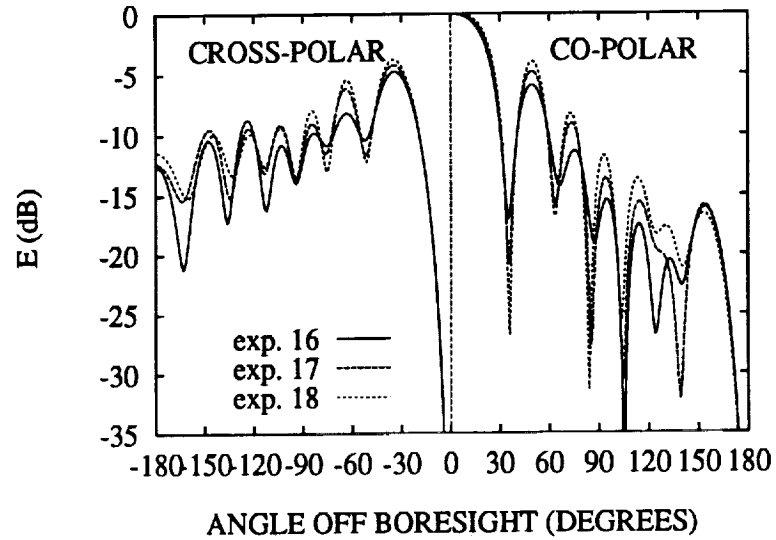


Figure 4.20: Variation of D -Plane pattern of LTSA's with α .

Plane. However, an interesting behavior is observed for short antennas when the total height of the antenna is larger than the length. In these cases, the maximum in the E -Plane radiation pattern is not obtained in the boresight direction. These cases are marked with * in Table 4.1. For short antennas, the current does not have the traveling wave nature in x -direction any more. When individual segment currents in x and z directions are considered for the LTSA geometry, a similarity to the skewed linear antenna can be a possible explanation for this behavior. Depending on the included angle, the skewed line antenna can create a radiation pattern which has a maximum at a direction other than boresight. When the length of the antenna is further reduced, maxima of the computed patterns are obtained in the D Plane and in the

cross polarized direction (cases 19 to 27). This observation is again attributed to the fact that the radiation due to z directed currents are more important than x directed currents. These cases are marked with ** in Table 4.1. The behavior of the antenna as a function of L is demonstrated in Figures 4.21 and 4.22.

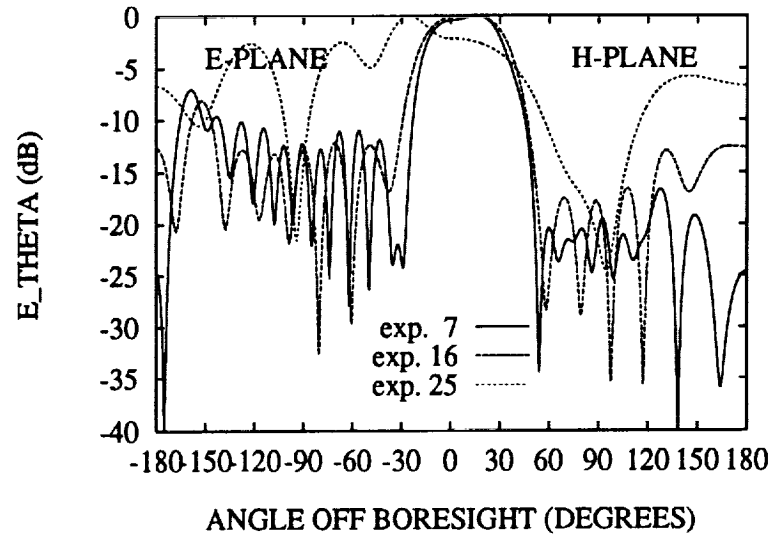


Figure 4.21: Variation of E and H -Plane patterns of LTSA's with L .

In general, it is observed that the peak cross polarization level of the antenna is quite high for the cases considered. However, it is interesting to note that a better radiation pattern can be obtained by decreasing the antenna height for a fixed L and α . Another interesting observation is that somewhat better antenna characteristics can still be obtained for short antennas ($L = \lambda$, for example) by keeping the antenna

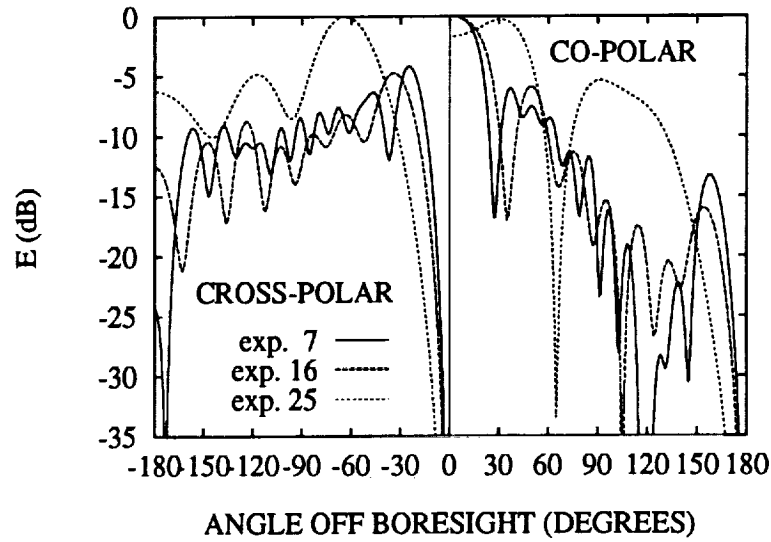


Figure 4.22: Variation of *D*-Plane pattern of LTSA's with *L*.

height small as well. This way, although the sidelobe levels and the cross polarization level are not as small as one can obtain from a longer antenna, the maximum is still attained in the boresight direction in the *E*-Plane. For array applications, this might be a useful design criterion since the sidelobe and cross polarization levels and beamwidth heavily depend on the array factor of the structure as well.

4.4 Computed Results for Dielectric Tapered Slot Antennas

In this section, sample results for dielectric LTSA's will be given. In order to investigate the effect of the dielectric permittivity, the same antenna geometry with a

receiving diode is computed with three different permittivities of the dielectric support. The results with the antenna parameters are given in Figures 4.23 and 4.24.

It is seen that, as the permittivity increases the E and H -Plane pattern sidelobe

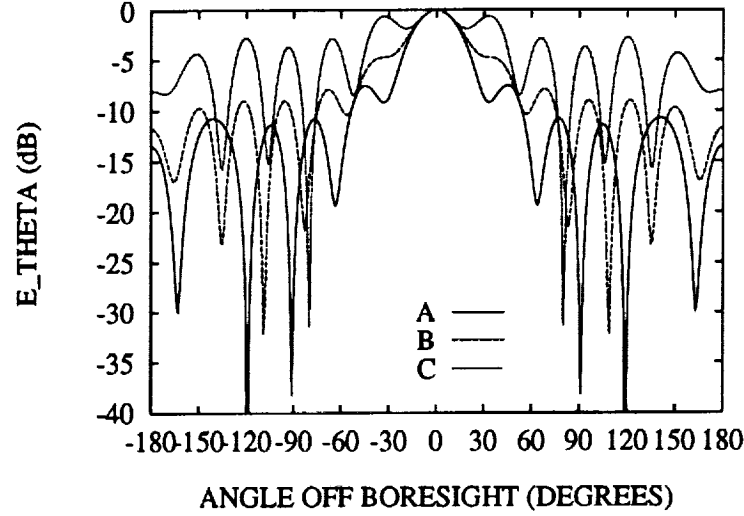


Figure 4.23: Variation of the E-Plane pattern for LTSA's with ϵ_r . A: $\epsilon_r = 2.33$, B: $\epsilon_r = 4.0$, C: $\epsilon_r = 5.0$ ($L = 2.0\lambda_0$, $H = 0.4\lambda_0$, $W_f = 0.01\lambda_0$, $d = 0.03\lambda_0$, $\alpha = 5$ degrees).

levels increase. The 3 dB beamwidth in the E -Plane remains essentially the same for this particular antenna geometry, whereas the H -Plane pattern beamwidth decreases. This should be expected since a higher percentage of the radiated power is trapped in the dielectric region of the antenna as the permittivity increases. Also, with increasing permittivity, the H -Plane pattern becomes more asymmetrical.

The analysis of the antenna of Figure 4.23 with $\epsilon_r = 2.33$ with changing dielectric thickness is shown in Figures 4.25 and 4.26. The same kind of behavior is observed

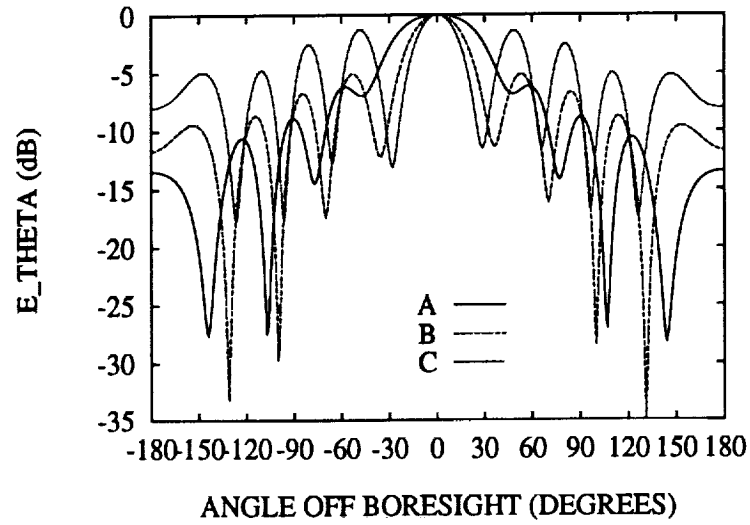


Figure 4.24: Variation of the H-Plane pattern for LTSA's with ϵ_r . A: $\epsilon_r = 2.33$, B: $\epsilon_r = 4.0$, C: $\epsilon_r = 5.0$ ($L = 2.0\lambda_0$, $H = 0.4\lambda_0$, $W_f = 0.01\lambda_0$, $d = 0.03\lambda_0$, $\alpha = 5$ degrees).

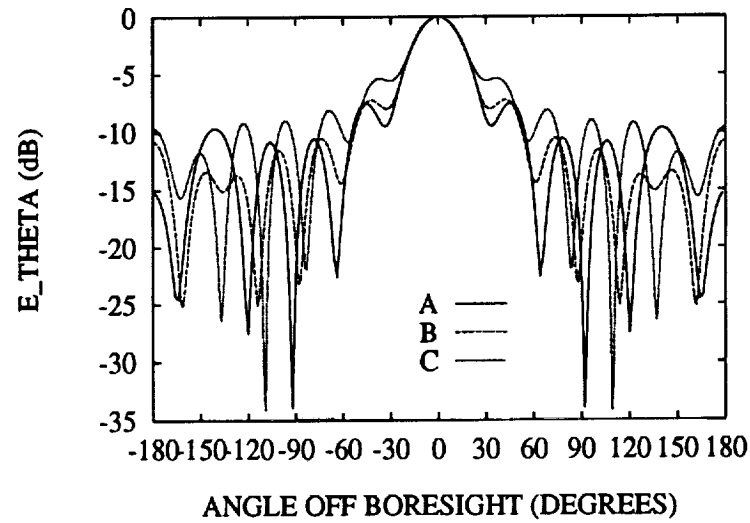


Figure 4.25: Variation of the E-Plane pattern for LTSA's with dielectric thickness, d . A: $d = 0.02\lambda_0$, B: $d = 0.06\lambda_0$, C: $d = 0.1\lambda_0$ ($\epsilon_r = 2.33$, $L = 2.0\lambda_0$, $H = 0.4\lambda_0$, $W_f = 0.01\lambda_0$, $\alpha = 5$ degrees).

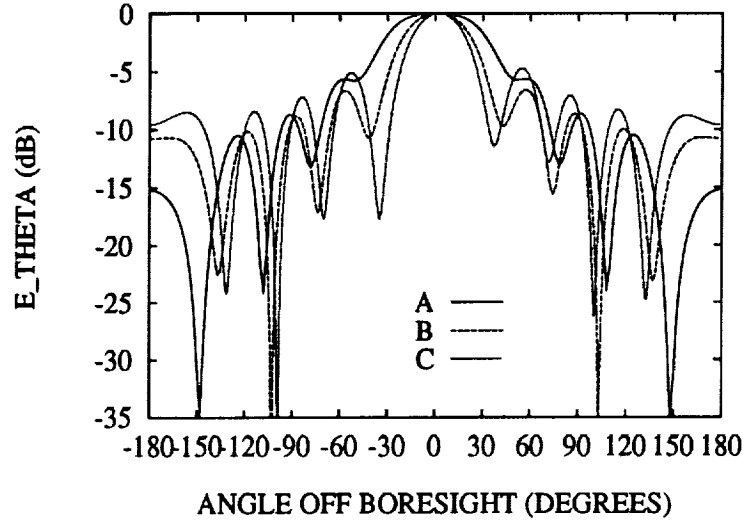


Figure 4.26: Variation of the H-Plane pattern for LTSA's with dielectric thickness, d . A: $d = 0.02\lambda_0$, B: $d = 0.06\lambda_0$, C: $d = 0.1\lambda_0$ ($\epsilon_r = 2.33$, $L = 2.0\lambda_0$, $H = 0.4\lambda_0$, $W_f = 0.01\lambda_0$, $\alpha = 5$ degrees).

with increasing dielectric thickness as with the increasing permittivity. However, in this case the variation in the sidelobe levels is not so large, a fact resulting from the small value of ϵ_r . To demonstrate this effect, a high permittivity antenna ($\epsilon_r = 9.8$) with changing dielectric thickness is analyzed and the results are shown in Figures 4.27 and 4.28. In this case, the effects are much more pronounced than the low permittivity case of Figures 4.25 and 4.26. These observations follow those reported in [4].

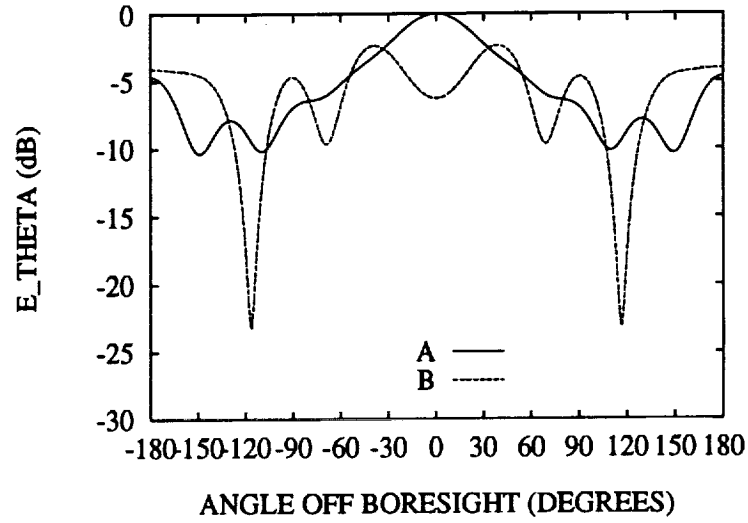


Figure 4.27: Variation of the E-Plane pattern for LTSA's with dielectric thickness, d , high ϵ_r case. A: $d = 0.02\lambda_0$, B: $d = 0.04\lambda_0$ ($\epsilon_r = 9.8$, $L = 1.05\lambda_0$, $H = 0.38\lambda_0$, $W_f = 0.004\lambda_0$, $\alpha = 5.7$ degrees).

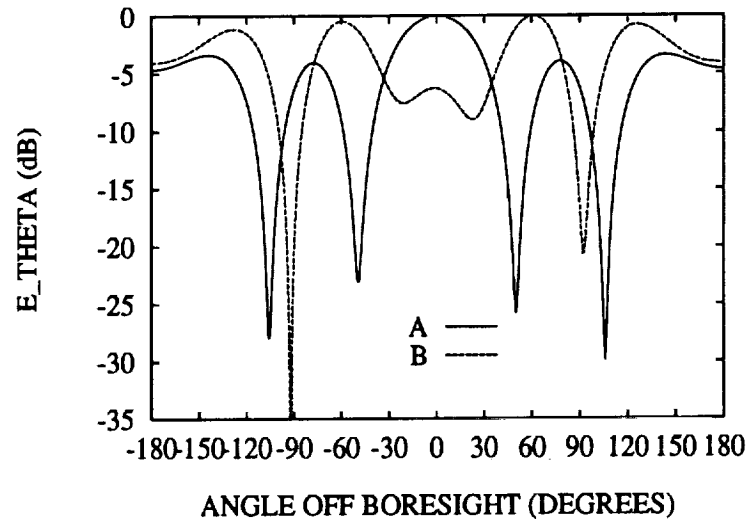


Figure 4.28: Variation of the H-Plane pattern for LTSA's with dielectric thickness, d , high ϵ_r case. A: $d = 0.02\lambda_0$, B: $d = 0.04\lambda_0$ ($\epsilon_r = 9.8$, $L = 1.05\lambda_0$, $H = 0.38\lambda_0$, $W_f = 0.004\lambda_0$, $\alpha = 5.7$ degrees).

CHAPTER 5

COMPUTER CODE AND PERFORMANCE

5.1 Code

The block diagram of the code is shown in Figure 5.1. In the main program, **struc**, the geometry of the antenna is entered and the type of feeding is chosen. Subroutine **mom** calls the impedance matrix filling subroutines **filcc**, **filcd**, **fildc** and **fildd**. These calculate the conductor-conductor, conductor-dielectric, dielectric-conductor and dielectric-dielectric interactions respectively. **filvlt** calculates the right hand side vector of the MoM matrix equation (2.22). The matrix equation is solved by the **cgrad** routine which utilizes the conjugate gradient method of Chapter 3. Organization of the input and output files of the code and the listings of the routines can be found in the appendix (under separate cover).

5.2 CPU Time and Memory Requirements

Since large matrices result in the analysis, the performance of the code is optimized by both approximations in the calculations and by vectorization. The final version of the

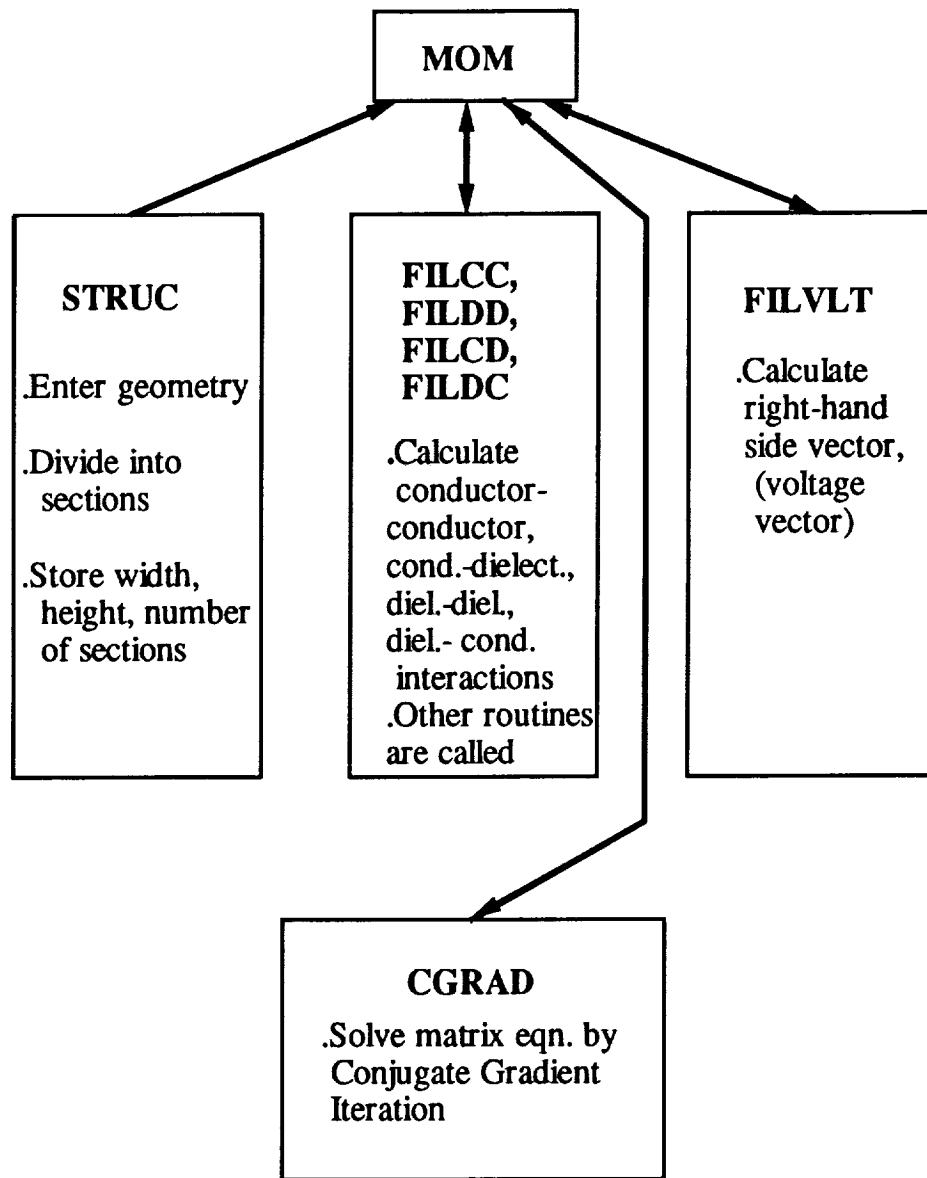


Figure 5.1: Block Diagram of the Code

code is adapted to and run on CRAY Y-MP of the North Carolina Supercomputing Center. The cost analysis of the code is carried out in order to estimate the necessary run times. For N conductor current unknowns and M dielectric polarization current

density unknowns, the matrix filling cost (FC) is given by

$$FC = O(N)n + O(NM)n + O(NM)nm + O(M)s \text{ Flops} \quad (5.1)$$

where n is the number of integration points, m is the number of subdivisions used in the computation of the dielectric-conductor interaction submatrix and s is the number of divisions used in the dielectric to dielectric interaction approximations. It is seen from (5.1) that FC is linearly proportional to $(N + M)$, the total number of unknowns.

The solution cost (SC) is given a

$$SC \leq \frac{(N + M)^3}{3} \text{ Flops} . \quad (5.2)$$

As mentioned earlier in Section 3.8, $(N + M)^3/3$ is the upper limit of SC . For most of the cases analyzed using the code, SC was much smaller than this limit because of the dominant diagonal of the resulting MoM matrix.

The performance of the code is monitored and enhanced throughout the work. Figure 5.2 shows the matrix fill time and the solution time of the code on Vector Alliant FX-40. The filling time increases linearly as predicted by (5.1), whereas the solution time increases faster, dominating the CPU time usage after about 400 unknowns. Figure 5.3 shows the comparison for the same cases analyzed using Alliant FX-40 and CRAY Y-MP. The big difference in the total run times in this figure results from the vectorization of the code and the high speed of the CRAY Y-MP

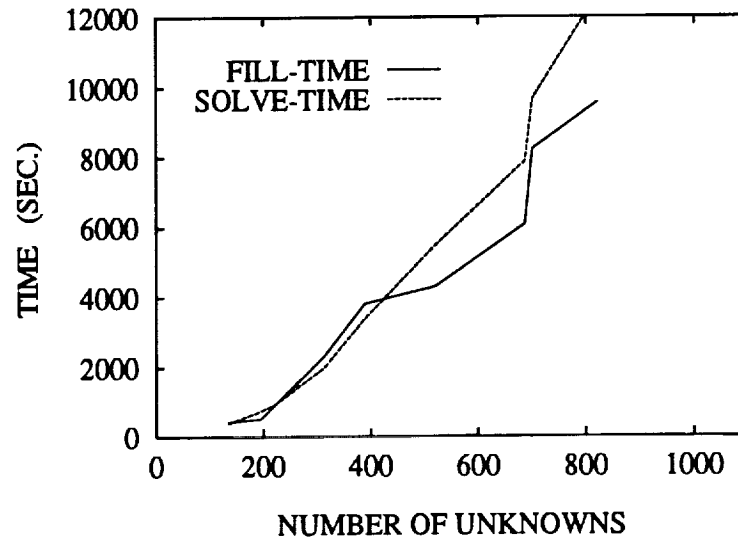


Figure 5.2: Matrix fill-time and solve time on Alliant FX-40 for air LTSA's

supercomputer. Another influencing factor is that the CRAY Y-MP is an actual memory machine, so that no time is lost for array reading and writing to and from the disk. Figure 5.4 shows the total run time as a function of number of unknowns for the dielectric LTSA's. All of these cases were calculated on the CRAY Y-MP because of the large CPU time that would be required otherwise. Here, it is worthwhile to note that the vectorization of the solution part of the code resulted in nearly linear behavior of the computation time instead of a higher power close to 3.

The limiting value of the number of unknowns in the method is set to be about $N + M = 5000$, where in a typical analysis $N = 1000$, and $M = 4000$. The run time memory requirement for this limit is approximately 26 MWords. All cases analyzed using the code resulted in less number of unknowns than 5000, and hence less mem-

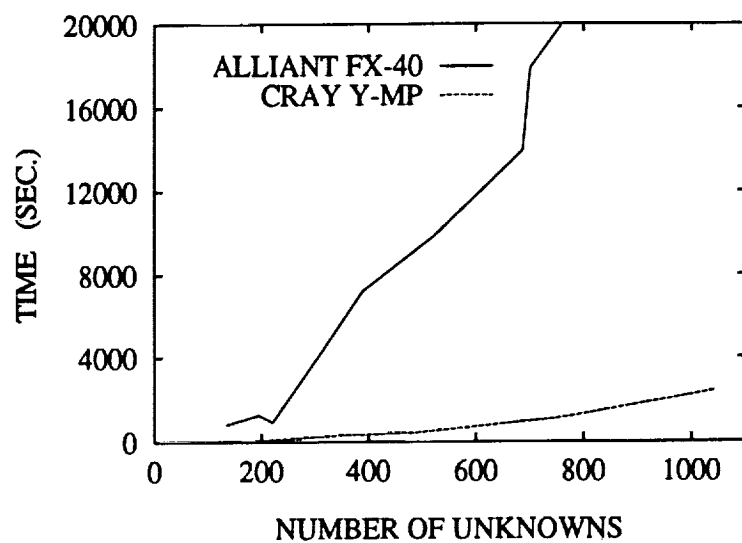


Figure 5.3: Total CPU time comparison for air LTSA's

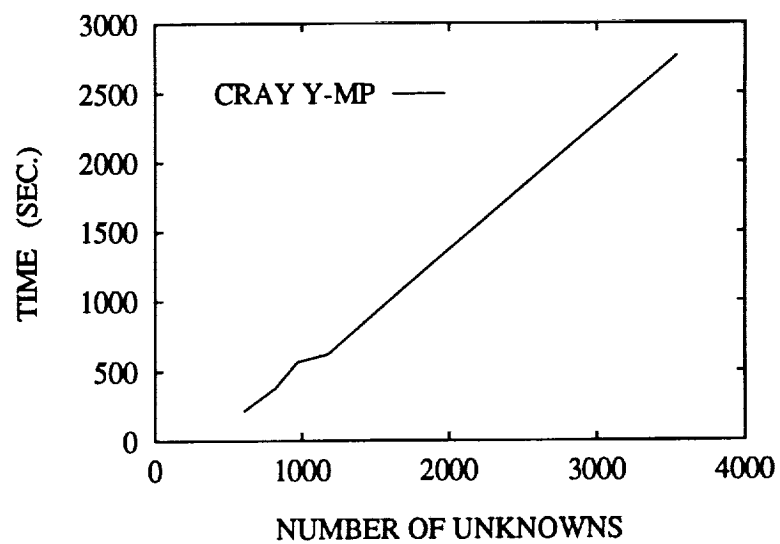


Figure 5.4: CPU time on CRAY Y-MP for dielectric LTSA's

ory requirement. The largest case that is analyzed using the code is the experimental dielectric LTSA of Chapter 4, which resulted in about 4000 unknowns. For higher permittivity dielectrics than that was used in the experiment, ($\epsilon_r = 2.33$), one would need more subdivisions in the dielectric. This, in turn, would reduce the solvable antenna dimensions. Therefore, as the permittivity increases, smaller antennas can be analyzed accurately with the code. Also, increasing the dielectric thickness would have the same effect since more segments than one would be needed across the thickness (y direction) of the dielectric. However, these statements are valid for current computational abilities and with the future developments in computer technology the solution of bigger problems with similar methods will be possible and less costly.

CHAPTER 6

CONCLUSIONS AND SUGGESTIONS FOR FUTURE WORK

In this work, a Method of Moments model for the analysis of the Linearly Tapered Slot Antenna is developed. The conducting parts of the antenna, including the feed section, are approximated closely for the first time. The finite dielectric region is modeled rigorously by including the equivalent volume polarization current density as an unknown in the formulation. The use of Schelkunoff's equivalence principle for the conducting region, together with the total field equality principle in the dielectric region, renders the problem into one which can be solved in free-space. As a result of this, the use of the particular Green's function and the associated approximations are avoided. The expansion functions are piecewise sinusoidal functions and unit pulses for conductor and dielectric regions respectively. Conductor basis functions are also used in the testing of the IE leading to a Galerkin type formulation for the conductor parts of the antenna. In the dielectric region, point matching is chosen to simplify the analysis.

The model is incorporated into a MoM code which can analyze LTSA's in air or

on a dielectric substrate, with a detector diode at the apex, or with a microstripline-to-slotline transition in the feed section. The code results are compared favorably to measurements and to available data in the literature. In order to check the approximation of the antenna taper by unequal size rectangular sectioning, the model is extended to analyze the skew-plate antenna and the results are favorably compared to a skew-segmentation model developed in this work. The variation of the radiation pattern with changing antenna parameters is investigated for the air TSA and the results are tabulated. It is observed that, narrower E -Plane beamwidths can be obtained as the antenna height, H , is reduced. Another important observation is that somewhat better antenna characteristics can be obtained for short antennas (small L), by reducing the antenna height (H) as well.

Since the matrix filling part of the MoM analysis is a major computational task, the computation time is reduced through the use of symmetry and the derivation of new simpler formulas for the mutual impedances of the perpendicular and parallel coplanar sinusoidal surface monopoles. Furthermore, the speed of the code is enhanced with vectorization of the matrix solution part of the algorithm, which employs a conjugate gradient iteration.

The model predicts the radiation characteristics of the LTSA with good accuracy. The unequal size rectangular sectioning scheme is a suitable approach converging to correct results by using approximately six segments per wavelength across the length and four to five segments per wavelength across the height of the antenna.

The computation times are realizable even for the largest antenna analyzed. The largest CPU time that is consumed by the code was about 2400 CPU seconds for $20\lambda_0^2$ air antenna, whereas the largest dielectric supported antenna ($15\lambda_0^2$) analysis consumed 3700 CPU seconds on CRAY Y-MP. Solvable problem size reduces with increasing dielectric permittivity, since more segments are required in the dielectric region because of the reduced slotline wavelength.

Suggestions for future work can be stated as:

- The CPU time requirements of the code can further be reduced by employing a table look-up algorithm in the matrix filling part of the code. This will also allow solution of larger structures.
- Another extension which can make possible the analysis of even larger problems is the employment of inhomogeneous sectioning for different parts of the antenna. The rectangular sectioning used in this work is homogeneous in the sense that the grid lines are equidistant. This approach is very simple and easy to implement as a computer code in terms of the identification of currents and the symmetry search for the impedance matrix calculations. However, not all parts of the antenna require the same grid for the same accuracy. For example, in the feed part of a microstripline fed antenna, more sections are required for both conductor and dielectric regions since the field is varying rapidly. Solution accuracy in this part of the antenna has a more important effect on the overall

solution compared to the sections farther away in the tapered region, since the wavelength in the slotline becomes larger. The same considerations also apply to the segments right near the taper and away from it. Therefore, the use of smaller sections in the feed part of the antenna and in the regions neighboring the taper, and larger sections elsewhere will yield smaller matrix sizes compared to homogeneous sectioning. However, the effect of this approach on the overall impedance matrix filling time should be studied.

- Only LTSA's are considered in this work. However, the developed model can be extended to handle other antenna structures as well. A natural extension of this work would be to analyze exponentially tapered slot antennas which have similar characteristics to the LTSA. A comparison between the two antennas with a parametric study (such as the one carried out in this work) would be very useful to the designers in the field. In particular, the cross-polarization level comparison can be very important, since the cross-polarization of the LTSA is quite high. Another modified structure of interest is a bi-slotline antenna which consists of two conducting sheets each having the same geometry as the single TSA, separated by a dielectric stub. This antenna can also be fed by a microstripline-to-bi-slotline transition. However, since the microstrip feed is contained in the structure, better sidelobe and cross-polarization levels can be obtained.

- Finally, with further modifications, the code can be specialized to other antenna types such as printed bi-conical antennas (provided that the antenna edges make small angles), and microstrip antennas.

REFERENCES

- [1] P.J.Gibson, "The Vivaldi Aerial," in *Proc. 9th European Microwave Conf.* (Brighton, U.K.), 1979, pp. 101-105.
- [2] S.N.Prasad and S.Mahapatra, "A Novel MIC Slot-Line Antenna," in *Proc. 9th European Microwave Conf.* (Brighton, U.K.), 1979, pp. 120-124.
- [3] K.S.Yngvesson, et al., "Endfire Tapered Slot Antennas on Dielectric Substrates," *IEEE Trans. Antennas Propagat.*, vol. AP-33, pp. 1392-1400, Dec. 1985.
- [4] R.Janaswamy, "Radiation Pattern Analysis of the Tapered Slot Antenna," Ph.D. dissertation, Univ. Massachusetts, 1986.
- [5] R.Janaswamy, Personal Communication, 1991.
- [6] R.Janaswamy, D.H.Schaubert and D.M.Pozar, "Analysis of the Transverse Electromagnetic Mode Linearly Tapered Slot Antenna," *Radio Science*, vol. 21, pp. 797-804, Oct. 1986.
- [7] R.Janaswamy and D.H.Schaubert, "Analysis of the Tapered Slot Antenna," *IEEE Trans. Antennas Propagat.*, vol. AP-35, pp. 1058-1064, Sept. 1987.
- [8] K.S.Yngvesson, et al., "A New Integrated Slot Element Feed Array for Multi-beam Systems," *IEEE Trans. Antennas Propagat.*, vol. AP-34, pp. 1372-1376, Nov. 1986.
- [9] J.F.Johansson, "A Moment Method Analysis of Linearly Tapered Slot Antennas," *AP-S/URSI Conference Proc.*, pp. 383-387, June 1989.
- [10] R.Janaswamy, "An Accurate Moment Method Model for the Tapered Slot Antenna," *IEEE Trans. Antennas Propagat.*, vol. AP-37, pp. 1523-1528, Dec. 1989.
- [11] U.Kotthaus and B.Vowinkel, "Investigation of Planar Antennas for Submillimeter Receivers," *IEEE Trans. Microwave Theory Tech.*, vol. MTT-37, pp. 375-380, Feb. 1989.

- [12] K.S.Yngvesson et al, "The Tapered Slot Antenna - A New Integrated Element for Millimeter-Wave Applications," *IEEE Trans. Microwave Theory Tech.*, vol. MTT-37, pp. 365-374, Feb. 1989.
- [13] R.L.Carrel, "The Characteristic Impedance of Two Infinite Cones of Arbitrary Cross Section," *IRE Trans. Antennas Propagat.*, vol. AP-6, pp. 197-201, May 1958.
- [14] S.A.Schelkunoff and H.T.Friis, *Antennas, Theory and Practice*, New York: Wiley, 1952.
- [15] R.Janaswamy and D.H.Schaubert, "Characteristic Impedance of a Wide Slotline on Low-Permittivity Substrates," *IEEE Trans. Microwave Theory Tech.*, vol. MTT-34, pp. 900-902, Aug. 1986.
- [16] A.Köksal and J.F.Kauffman, "Moment Method Analysis of Linearly Tapered Slot Antennas," *IEEE AP-S URSI Symposium Digest*, vol. 1, pp. 314-317, June 24-28, 1991, London, Ontario-Canada
- [17] E.K.Miller, "A Selective Survey of Computational Electromagnetics," *IEEE Trans. Antennas Propagat.*, vol. AP-36, pp. 1281-1305, Sept. 1988.
- [18] B.H.McDonald and A.Wexler, "Finite-Element Solution of Unbounded Field Problems," *IEEE Trans. Microwave Theory Tech.*, vol. MTT-20, pp. 841-847, Dec. 1972.
- [19] R.F.Harrington, "Matrix Methods for Field Problems," *Proc. IEEE*, vol. 55, pp. 136-149, Feb. 1967.
- [20] R.F.Harrington, *Field Computation by Moment Methods*, New York: Macmillan, 1968.
- [21] T.K.Sarkar, "The Conjugate Gradient Technique as Applied to Electromagnetic Field Problems," *IEEE AP-S Newsletter*, vol. 28, No. 4, pp. 5-14, 1986.
- [22] T.K.Sarkar, E.Arvas and S.M.Rao, "Applications of FFT and Conjugate Gradient Method for the Solution of Electromagnetic Radiation from Electrically Large and Small Conducting Bodies," *IEEE Trans. Antennas Propagat.*, vol. AP-33, pp. 635-640, 1986.
- [23] M.F.Catedra, J.A.Alcaraz and J.C.Arredondo, "Analysis of Arrays of Vivaldi and LTSA Antennas," *AP-S/URSI Conference Proc.*, pp. 123-124, June 1989.
- [24] D.M.Pozar, "Input Impedance and Mutual Coupling of Rectangular Microstrip Antennas," *IEEE Trans. Antennas Propagat.*, vol. AP-30, pp. 1191-1196, Nov. 1982.

- [25] N.N.Wang, J.H.Richmond and M.C.Gilreath, "Sinusoidal Reaction Formulation for Radiation and Scattering from Conducting Surfaces," *IEEE Trans. Antennas Propagat.*, vol. AP-23, pp. 376-382, May 1975.
- [26] D.E.Livesay and K.Chen, "Electromagnetic Fields Induced Inside Arbitrarily Shaped Biological Bodies," *IEEE Trans. Microwave Theory Tech.*, vol. MTT-22, pp. 1273-1280, Dec 1974.
- [27] T.K.Sarkar, E.Arvas and S.Ponnappalli, "Electromagnetic Scattering from Dielectric Bodies," *IEEE Trans. Antennas Propagat.*, vol. AP-37, pp. 673-676, May 1989.
- [28] E.H.Newman and P.Tulyathan, "Wire Antennas in the Presence of a Dielectric/Ferrite Inhomogeneity," *IEEE Trans. Antennas Propagat.*, vol. AP-26, pp. 587-593, July 1978.
- [29] T.K.Sarkar and E.Arvas, "An Integral Equation Approach to the Analysis of Finite Microstrip Antennas: Volume/Surface Formulation," *IEEE Trans. Antennas Propagat.*, vol. AP-38, pp. 305-312, March 1990.
- [30] A.W.Glisson and D.R.Wilton, "Simple and Efficient Numerical Methods for Electromagnetic Radiation and Scattering from Surfaces," *IEEE Trans. Antennas Propagat.*, vol. AP-28, pp.593-603, Sept. 1980.
- [31] S.M.Rao, D.R.Wilton and A.W.Glisson, "Electromagnetic Scattering by Surfaces of Arbitrary Shape," *IEEE Trans. Antennas Propagat.*, vol. AP-30, pp.409-418, May 1982.
- [32] J.Singh and A.T.Adams, "A Nonrectangular Patch Model for Scattering from Surfaces," *IEEE Trans. Antennas Propagat.*, vol. AP-27, pp. 531-535, July 1979.
- [33] E.H.Newman and P.Tulyathan, "A Surface Patch Model for Polygonal Plates," *IEEE Trans. Antennas Propagat.*, vol. AP-30, pp. 588-593, July 1982.
- [34] E.H.Newman, P.Alexandropoulos and E.K.Walton, "Polygonal Plate Modeling of Realistic Structures," *IEEE Trans. Antennas Propagat.*, vol. AP-32, pp. 742-747, July 1984.
- [35] D.L.Knepp and J.Goldhirsh, "Numerical Analysis of Electromagnetic Radiation Properties of Smooth Conducting Bodies of Arbitrary Shape," *IEEE Trans. Antennas Propagat.*, vol. AP-19, pp. 383-388, May 1972.
- [36] E.H.Newman and D.M.Pozar, "Electromagnetic Modeling of Composite Wire and Surface Geometries," *IEEE Trans. Antennas Propagat.*, vol. AP-26, pp.784-789, Nov. 1978.

- [37] H.E.King, "Mutual Impedances of Unequal Length Antennas in Echelon," *IRE Trans. Antennas Propagat.*, vol. AP-5, pp. 306-313, July 1957.
- [38] J.H.Richmond and N.H.Geary, "Mutual Impedance Between Coplanar-Skew Dipoles," *IEEE Trans. Antennas Propagat.*, vol. AP-18, pp. 414-416, May 1970.
- [39] E.H.Newman and D.M.Pozar, "Considerations for Efficient Wire/Surface Modeling," *IEEE Trans. Antennas Propagat.*, vol. AP-28, pp. 121-125, Jan. 1980.
- [40] R.Janaswamy, "A Simplified Expression for the Self/Mutual Impedance between Coplanar and Parallel Surface Monopoles," *IEEE Trans. Antennas Propagat.*, vol. AP-35, pp. 1174-1176, Oct. 1987.
- [41] G.Davis, "An Expression for the Mutual Impedance of Coplanar, Orthogonal Surface Patches," *IEEE Trans. Antennas Propagat.*, vol. AP-38, pp. 1975-1978, Dec. 1990.
- [42] A.Köksal and J.F.Kauffman, "Mutual Impedance of Parallel and Perpendicular Coplanar Surface Monopoles," *IEEE Trans. Antennas Propagat.*, vol. AP-39, pp. 1251-1256, Aug. 1991.
- [43] D.H.Schaubert, D.R.Wilton and A.W.Glisson, "A Tetrahedral Modeling Method for Electromagnetic Scattering by Arbitrarily Shaped Inhomogeneous Dielectric Bodies," *IEEE Trans. Antennas Propagat.*, vol. AP-32, pp. 77-85, Jan. 1984.
- [44] M.C.Bailey and M.D.Desphande, "Integral Equation Formulation of Microstrip Antennas," *IEEE Trans. Antennas Propagat.*, vol. AP-30, pp. 651-656, July 1982.
- [45] M.D.Desphande and M.C.Bailey, "Input Impedance of Microstrip Antennas," *IEEE Trans. Antennas Propagat.*, vol. AP-30, pp. 645-651, July 1982.
- [46] D.M.Pozar and S.M.Voda, "A Rigorous Analysis of a Microstripline Fed Patch Antenna," *IEEE Trans. Antennas Propagat.*, vol. AP-35, pp. 1343-1349, Dec. 1987.
- [47] A.J.Poggio and E.K.Miller, "Integral equation solutions of three-dimensional scattering problem, in" *Techniques for Electromagnetics*, R.Mitra, Ed. Elmsford, NY: Pergamon, 1973
- [48] A.W.Glisson, "An Integral Equation for Electromagnetic Scattering from Homogeneous Dielectric Bodies," *IEEE Trans. Antennas Propagat.*, vol. AP-32, pp. 173-175, Feb. 1984.
- [49] A.D.Yaghjian, "Electric Dyadic Green's Functions in the Source Region," *Proceedings of the IEEE*, vol. 68, pp. 248-263, Feb. 1980.

- [50] J.B.Knorr, "Slot-Line Transitions," *IEEE Trans. Microwave Theory Tech.*, vol. MTT-22, pp. 548-554, May 1974.
- [51] M.R.Hestenes and E.Stiefel, "Methods of Conjugate Gradients for Solving Linear Systems," *J. Res. Nat. Bur. Standards*, vol. 49, pp. 409-436, Dec.1952.
- [52] J.W.Daniel, "The Conjugate Gradient Method for Linear and Nonlinear Operator Equations," *SIAM J. Numer. Anal.*, vol. 4, No.1, pp. 10-26, 1967.
- [53] T.K.Sarkar, "On the Application of the Generalized BiConjugate Gradient Method," *Journal of Electromagn. Waves and App.*, vol. 1, No. 3, pp. 223-242, 1987.
- [54] T.K.Sarkar, K.R.Siarkiewicz and R.F.Stratton, "Survey of Numerical Methods for Solution of Large Systems of Linear Equations for Electromagnetic Field Problems," *IEEE Trans. Antennas Propagat.*, vol. AP-29, pp. 847-856, Nov. 1981.
- [55] T.K.Sarkar and E.Arvas, "On a Class of Finite Step Iterative Methods (Conjugate Directions) for the Solution of an Operator Arising in Electromagnetics," *IEEE Trans. Antennas Propagat.*, vol. AP-33, pp. 1058-1066, Oct. 1985.
- [56] A.C.Ludwig, "The Definition of Cross Polarization," *IEEE Trans. Antennas Propagat.*, vol. AP-21, No. 1, pp. 116-119, Jan. 1973.

Public reporting burden for this collection of data is estimated to average 1 hour per response, including the time for reviewing instructions, searching existing data sources, gathering and maintaining the data needed, and completing and reviewing the collection of information. Send comments regarding this burden estimate or any other aspect of this collection of information, including suggestions for reducing this burden, to Washington Headquarters Service, Directorate for Information Operations and Services, Paperwork Reduction Project (0704-0188), Washington, DC 20503.

1. AGENCY USE ONLY (Leave blank)		2. REPORT DATE June 1993		3. REPORT TYPE AND DATES COVERED Contractor Report	
4. TITLE AND SUBTITLE Moment Method Analysis of Linearly Tapered Slot Antennas				5. FUNDING NUMBERS G NAG1-943 WU 506-59-64-01	
6. AUTHOR(S) Adnan Koksal					
7. PERFORMING ORGANIZATION NAME(S) AND ADDRESS(ES) North Carolina State University Department of Electrical and Computer Engineering Raleigh, NC 27695				8. PERFORMING ORGANIZATION REPORT NUMBER	
9. SPONSORING / MONITORING AGENCY NAME(S) AND ADDRESS(ES) National Aeronautics and Space Administration Langley Research Center Hampton, VA 23681-0001				10. SPONSORING / MONITORING AGENCY REPORT NUMBER NASA CR-191474	
11. SUPPLEMENTARY NOTES Langley Technical Monitor: M. C. Bailey Final Report - Jan. 15, 1989 to Sept. 30, 1991					
12a. DISTRIBUTION / AVAILABILITY STATEMENT Unclassified-Unlimited Subject Category 15				12b. DISTRIBUTION CODE	
13. ABSTRACT (Maximum 200 words) A Method of Moments (MoM) model for the analysis of the Linearly Tapered Slot Antenna (LTSA) is developed and implemented. The model employs an unequal size rectangular sectioning for conducting parts of the antenna. Piecewise sinusoidal basis functions are used for the expansion of conductor current. The effect of the dielectric is incorporated in the model by using equivalent volume polarization current density and solving the equivalent problem in free-space. The feed section of the antenna including the microstripline is handled rigorously in the MoM model by including slotline short circuit and microstripline currents among the unknowns. Comparison with measurements is made to demonstrate the validity of the model for both the air case and the dielectric case. Validity of the model is also verified by extending the model to handle the analysis of the skew-plate antenna and comparing the results to those of a skew-segmentation modeling results of the same structure and to available data in the literature. Variation of the radiation pattern for the air LTSA with length, height, and taper angle is investigated, and the results are tabulated. Numerical results for the effect of the dielectric thickness and permittivity are presented.					
14. SUBJECT TERMS MoM code, antenna radiation pattern, Linear Tapered Slot Antenna (LTSA)				15. NUMBER OF PAGES 95	
				16. PRICE CODE A05	
17. SECURITY CLASSIFICATION OF REPORT Unclassified		18. SECURITY CLASSIFICATION OF THIS PAGE Unclassified		19. SECURITY CLASSIFICATION OF ABSTRACT	
20. LIMITATION OF ABSTRACT					